

SOLVING ATOMIC STRUCTURE USING STATISTICAL MECHANICAL SEARCHES ON
X-RAY SCATTERING DERIVED POTENTIAL ENERGY SURFACES

by

Christopher James Wright

Bachelor of Science
Brown University 2014

Submitted in Partial Fulfillment of the Requirements

for the Degree of Masters of Science in

Chemical Engineering

College of Engineering and Computing

University of South Carolina

2016

Accepted by:

Xiao-Dong Zhou, Major Professor

Thomas Vogt, Committee Member

Mark Uline, Committee Member

Jochen Lauterbach, Committee Member

Lacy Ford, Vice Provost and Dean of Graduate Studies

© Copyright by Christopher James Wright, 2016
All Rights Reserved.

DEDICATION

ACKNOWLEDGMENTS

ABSTRACT

TABLE OF CONTENTS

DEDICATION	iii
ACKNOWLEDGMENTS	iv
ABSTRACT	v
LIST OF TABLES	ix
LIST OF FIGURES	x
TODO LIST	1
CHAPTER 1 ATOMIC STRUCTURE: EXTRACTION AND APPLICATION . . .	3
1.1 Atomistic Goals	3
1.2 Atomistic Experiments	4
1.3 Atomistic Simulations	4
CHAPTER 2 STATISTICAL MECHANICAL ENSEMBLES AND POTENTIAL ENERGY SURFACES	5
2.1 Introduction	5
2.2 Potential Energy Surfaces	5
2.3 Ensembles	7

CHAPTER 3 ATOMIC PAIR DISTRIBUTION FUNCTION: THEORY AND COMPUTATION	12
3.1 Theory	12
3.2 Computation	14
3.3 Experiment	17
3.4 Data Processing Workflow	18
CHAPTER 4 BENCHMARKING	35
4.1 PDF	35
4.2 PDF with ADPs	35
CHAPTER 5 ANNEALING AND AGGREGATION OF 2NM AU NANOPARTICLES	41
5.1 Experiments	41
5.2 Data Processing	41
5.3 Data Analysis	41
5.4 Simulation	41
5.5 Structural Analysis	41
5.6 Conclusions	41
CHAPTER 6 PHASE CHANGES AND ANNEALING DYNAMICS OF Pr_2NiO_4 AND ITS DERIVATIVES	42
6.1 Experiments	42
6.2 Data Processing	42
6.3 Data Analysis	42
6.4 Simulation	42

6.5 Structural Analysis	42
6.6 Conclusions	42
CHAPTER 7 CONCLUSION	43

LIST OF TABLES

LIST OF FIGURES

Figure 3.1 Comparison of the CPU and GPU chip architectures	15
Figure 3.2 Database Loading Workflow. Data is loaded from various sources, including images and text files, into the FileStore and Meta-dataStore databases. Data is then retrieved from the databases using the databroker.	18
Figure 3.3 Scattering onto a flat detector	19
Figure 3.4 Q resolution as a function of Q	20
Figure 3.5 Number of pixels as a function of Q , binned at the Q resolution of the detector.	21
Figure 3.6 Generated dead/hot pixel masks for a detector with 100 bad pixels. a) the standard even bin mask and b) the Q resolution binned mask. The bad pixels are noted with open circles, masked pixels are noted with closed circles.	23
Figure 3.7 Generated dead/hot pixel masks for a detector with 300 bad pixels. a) the standard even bin mask and b) the Q resolution binned mask. The bad pixels are noted with open circles, masked pixels are noted with closed circles.	24
Figure 3.8 Generated dead/hot pixel masks for a detector with 500 bad pixels. a) the standard even bin mask and b) the Q resolution binned mask. The bad pixels are noted with open circles, masked pixels are noted with closed circles.	24
Figure 3.9 Generated dead/hot pixel masks for a detector with 1000 bad pixels. a) the standard even bin mask and b) the Q resolution binned mask. The bad pixels are noted with open circles, masked pixels are noted with closed circles.	25
Figure 3.10 Generated beamstop holder masks for a beamstop holder with 10% transmittance. a) the raw image, b) the masked image, c) and the missed pixels	25

Figure 3.11 Generated beamstop holder masks for a beamstop holder with 30% transmittance. a) the raw image, b) the masked image, c) and the missed pixels	26
Figure 3.12 Generated beamstop holder masks for a beamstop holder with 50% transmittance. a) the raw image, b) the masked image, c) and the missed pixels	26
Figure 3.13 Generated beamstop holder masks for a beamstop holder with 90% transmittance. a) the raw image, b) the masked image, c) and the missed pixels	26
Figure 3.14 Generated beamstop holder masks which is rotated away from verticle	27
Figure 3.15 Masked experimental data. a) the raw image, b) the mask	27
Figure 3.16 Masked experimental data with Pt single crystal signal. a) the raw image, b) the mask	28
Figure 3.17 Masked experimental data with Pt single crystal signal using figure's 3.15 as a starting mask. a) the raw image, b) the mask	28
Figure 3.18 Masking, average, and standard deviation of an example x-ray total scattering measurement. This image was produced with no mask. a) the image, b) the mask, c) the mean and median values, d) the standard deviation (normalized to the median), e) a closeup of the 28 \AA^{-1} to $31 \text{ \AA}^{-1}Q$ range for the mean and median, f) 28 \AA^{-1} to $31 \text{ \AA}^{-1}Q$ range for the standard deviation	32
Figure 3.19 Masking, average, and standard deviation of an example x-ray total scattering measurement. This image was produced with only an edge mask. a) the image, b) the mask, c) the mean and median values, d) the standard deviation (normalized to the median), e) a closeup of the 28 \AA^{-1} to $31 \text{ \AA}^{-1}Q$ range for the mean and median, f) 28 \AA^{-1} to $31 \text{ \AA}^{-1}Q$ range for the standard deviation	33
Figure 3.20 Masking, average, and standard deviation of an example x-ray total scattering measurement. This image was produced combining an edge mask and the automatically generated mask. a) the image, b) the mask, c) the mean and median values, d) the standard deviation (normalized to the median), e) a closeup of the 28 \AA^{-1} to $31 \text{ \AA}^{-1}Q$ range for the mean and median, f) 28 \AA^{-1} to $31 \text{ \AA}^{-1}Q$ range for the standard deviation	34

Figure 4.1 Au ₅₅ PDF fitting of DFT-optimized <i>c</i> -Au ₅₅ . a) the final structural solution ($R_w=0.3\%$) with bond lengths color-coded by step of 0.05Å, b) the target PDF(blue dots) overlaid with the PDF of the final structure (solid red lines) with the difference in green lines offset below, c) the radial bond distribution, and d) bond angle distribution.	36
Figure 4.2 Au ₅₅ PDF fitting of surface-disordered Au ₅₅ . a) the target structure, b) the final structural solution ($R_w=0.6\%$), c) the comparison of PDFs, d) the CN distribution with the number of atoms in either the core or the surface, e) the radial bond distribution, and f) the bond angle distribution.	37
Figure 4.3 Similar to figure 4.2 for DFT-optimized amorphous Au ₅₅	38
Figure 4.4 Similar to figure 4.2 for Au ₁₀₂ as in DFT-optimized Au ₁₀₂ MBA ₄₄ cluster.	39
Figure 4.5 Similar to Fig. 4.4 with Marks decahedron as the starting structure.	40

1

TODO LIST

INTRODUCTION

3 This is the introduction to the thesis.

CHAPTER 1

5 ATOMIC STRUCTURE: EXTRACTION AND APPLICATION

6 1.1 ATOMISTIC GOALS

7 The only way to truly understand the fundamental souce of material and chemical
8 properties is through atomic structure. The goal of atomistic engineering is to pro-
9 duce novel structures and combinations of structures to engender new properties and
10 functions. This includes producing stronger materials, more durable catalysts, more
11 energy dense batteries, and many more engineering applicatons. The true power of
12 atomistic engineering has been shown in biochemistry and pharmicuttical design. Al-
13 though the production of drugs and biomeical treatments is usually considered to be
14 rather far from the field of catalyst design and materials science, the atomistic nature
15 of these fields can not be denied. The field of protiene structural analysis stands
16 as an example of structural science, elcuidating the three dimensional coordinates of
17 thousands of atoms. These structures are then used to describe how the molecular
18 machinery of the biological world works, enabling the development of new drugs and
19 treatments for diseases and a deeper understanding of how we evolved. The develop-
20 ment of protene inhibitor drugs, which are important to so many treatments, would
21 have not been possible without very detailed atomic structures. The asperation of
22 this work is to create this level of accuracy and utility, generating structures which
23 allow for the understanding of how materials work on a fundamental level.

24 **1.2 ATOMISTIC EXPERIMENTS**

25 **Single Crystal Diffraction**

26 **Electron Microscopy**

27 **X-ray Total Scattering**

28 **1.3 ATOMISTIC SIMULATIONS**

29 The goals of atomistic simulations are usually to produce atomic structures from
30 quantum mechanical first principles, as in the case of Density Functional Theory
31 (DFT), or classical approximations to quantum mechanics.

32 **Density Functional Theory**

33 **Classical Force Field**

34 **Monte Carlo and Statistical Mechanics**

35 Maybe put the ensemble and PES work here, since it is more general than the PDF
36 per say. Also the rational for the gradients and fast computation make much more
37 sense knowing we are going to be very sample happy and follow the gradient of the
38 PES.

39

CHAPTER 2

40

STATISTICAL MECHANICAL ENSEMBLES AND POTENTIAL ENERGY SURFACES

42 2.1 INTRODUCTION

43 The approach taken in this work for solving the atomic structures of materials is
44 one of optimization. The positional variables of the system are optimized so as to
45 minimize the value of a potential energy surface (PES). The

46 2.2 POTENTIAL ENERGY SURFACES

47 A PES simply describes the potential energy of the system as a function of all its
48 relevant coordinates in phase space, essentially providing a mapping $\mathbb{R}^n \rightarrow \mathbb{R}$. Usually
49 these coordinates are the positions of the atoms q and their conjugate momenta p .
50 Note that there could be more variables associated with the system, for instance the
51 magnetic moments of the atoms could play a role in describing the system. In this
52 magnetic system there would be positional variables for the atomwise spin vectors
53 and their "momenta". Application of the term "momenta" might seem odd here, as
54 the magnetic spin does not have a mass or a velocity. However, since the magnetic
55 "position" is defined on the PES we need to describe its conjugate variable to properly
56 formulate Hamiltonian dynamics and the kinetic portion of the PES.

57 **Experimentally Derived Potential Energy Surfaces**

58 Generally PESs are obtained from purely computational experiments including: ab-
 59 initio DFT, classical approximations via the embedded atom method, or even param-
 60 eter driven models with experimentally fitted parameters. However, one can derive
 61 a PES from an experiment which describes how well the model reproduces the ex-
 62 perimental data. In this case one needs a theoretical and computational framework
 63 mapping the atomistic variables of the simulation to the same space of the data ob-
 64 tained from the experiment. This allows the experiment to be compared directly
 65 against the predicted data via an experimentally derived PES.

66 **Potentials**

67 For an experiment which produces 1D data, like powder diffraction, EXAFS or XPS,
 68 the implemented potentials are:

$$\chi^2 = \sum_{a=a_{\min}}^{a_{\max}} (A_{\text{obs}} - \alpha A_{\text{calc}})^2 \quad (2.1)$$

$$Rw = \sqrt{\frac{\sum_{a=a_{\min}}^{a_{\max}} (A_{\text{obs}} - \alpha A_{\text{calc}})^2}{\sum_{a=a_{\min}}^{a_{\max}} A_{\text{obs}}^2}} \quad (2.2)$$

$$\chi_{\text{INVERT}}^2 = \frac{1}{N} \sum_j \sum_r [A_{\text{obs}}(r) - \alpha A_{j,\text{calc}}(r)]^2 \quad (2.3)$$

$$\alpha = \frac{\sum_{a=a_{\min}}^{a_{\max}} A_{\text{obs}} A_{\text{calc}}}{\sum_{a=a_{\min}}^{a_{\max}} A_{\text{calc}}^2} = \frac{\vec{A}_{\text{obs}} \cdot \vec{A}_{\text{calc}}}{|\vec{A}_{\text{calc}}|^2} \quad (2.4)$$

72 where A_{calc} and A_{obs} are the calculated and observed 1D experimental data and $A_{\text{calc},j}$
 73 is the calculated data for a single atom interacting with the other atoms of the system.
 74 Note that A_{calc} has a dependence on q , the positions of the system.

75 **Forces**

$$\vec{\nabla} \chi^2 = -2 \sum_{a=a_{\min}}^{a_{\max}} (\alpha \frac{\partial A_{\text{calc}}}{\partial \gamma_{i,w}} + A_{\text{calc}} \frac{\partial \alpha}{\partial \gamma_{i,w}})(A_{\text{obs}} - \alpha A_{\text{calc}}) \quad (2.5)$$

76

$$\vec{\nabla}Rw = \frac{Rw}{\chi^2} \sum_{a=a_{\min}}^{a_{\max}} (\alpha \frac{\partial A_{\text{calc}}}{\partial \gamma_{i,w}} + A_{\text{calc}} \frac{\partial \alpha}{\partial \gamma_{i,w}})(\alpha A_{\text{calc}} - (A_{\text{obs}})) \quad (2.6)$$

77

$$\frac{\partial \alpha}{\partial \gamma_{i,w}} = \frac{(\sum_{a=a_{\min}}^{a_{\max}} A_{\text{obs}} \frac{\partial A_{\text{calc}}}{\partial \gamma_{i,w}} - 2\alpha \sum_{a=a_{\min}}^{a_{\max}} A_{\text{calc}} \frac{\partial A_{\text{calc}}}{\partial \gamma_{i,w}})}{\sum_{a=a_{\min}}^{a_{\max}} A_{\text{calc}}^2} \quad (2.7)$$

78

$$\vec{\nabla}\chi^2_{\text{INVERT}} = \frac{-2}{N} \sum_{a=a_{\min}}^{a_{\max}} \sum_j (\alpha \frac{\partial A_{j,\text{calc}}}{\partial \gamma_{i,w}} + A_{j,\text{calc}} \frac{\partial \alpha}{\partial \gamma_{i,w}})(A_{\text{obs}} - \alpha A_{j,\text{calc}}) \quad (2.8)$$

79 where $\gamma_{i,w}$ is the i th arbitrary positional variable in the w th direction. The concept
 80 of an "arbitrary positional variable" might seem a bit cumbersome but it allows us
 81 to define the forces for any atomic parameter which can be represented as a vector
 82 in 3-space. This comes in handy when trying to define the forces acting on variables
 83 like anisotropic displacement parameters or atomic magnetic spins.

84 DISCUSS INVERT A BUNCH. ALSO COMPARE RW AND CHI**2, POTEN-
 85 TIALY WITH A FIGURE.

86 2.3 ENSEMBLES

87 While PESs describe which atomic configurations are the most desirable and how
 88 the atoms would like to get there, the ensemble describes how the atoms move on
 89 the PES. The abstraction of the PES from the ensemble is an important one, as it
 90 allows for the reuse and exchange of both PESs and ensembles for a wide array of
 91 problems. Statistical mechanical ensembles can be described in two ways, analytically
 92 and stochastically. For long simulation times and fine enough numerical or analytical
 93 integration these two descriptions should be identical. In either case one starts by
 94 defining the Hamiltonian \mathcal{H} as the total energy of the system. Thus, the Hamiltonian
 95 is described as the sum of the potential $U(q)$ and kinetic $K(p)$ energies, where q is
 96 the positions of the atoms and p is their momenta

$$\mathcal{H}(q, p) = U(q) + K(p) \quad (2.9)$$

97 where $K(p) = \frac{1}{2} \sum_i \frac{p_i^2}{m_i}$ and i denotes the i th particle. Analytically one generally defines
 98 a partition function, which describes the sum of probabilities over all potential atomic
 99 states.

$$\Xi = \sum_i P_i(q, p)$$

100 where P_i is the probability of the i th state and is a function of the total energy of
 101 that state. This partition function can then be used to obtain the probability of any
 102 specific state.

103 Hamiltonian Monte Carlo

In order to model dynamics we need to describe the motion of the particles in our system, thus:

$$\frac{dq_i}{dt} = \frac{\partial \mathcal{H}}{\partial p_i} = p_i \quad (2.10)$$

$$\frac{dp_i}{dt} = -\frac{\partial \mathcal{H}}{\partial q_i} = -\vec{\nabla}U \quad (2.11)$$

Using these equations we can derive the position and momentum vectors at any point in time using the leap-frog algorithm:

$$p_i(t + \delta t/2) = p_i(t) - \frac{\delta t}{2} \frac{\partial}{\partial q_i} U(q(t)) \quad (2.12)$$

$$q_i(t + \delta t) = q_i(t) + \delta t * p_i(t + \delta t/2) \quad (2.13)$$

$$p_i(t + \delta t) = p_i(t + \delta t/2) - \frac{\delta t}{2} \frac{\partial}{\partial q_i} U(q(t + \delta t)) \quad (2.14)$$

104 Note that $\frac{\partial}{\partial q_i}$ is the gradient with respect to q where i denotes the i th atom being
 105 moved. Using this notation the gradient is

$$\vec{\nabla}U = \begin{bmatrix} \frac{\partial U}{\partial q_{0,x}} & \frac{\partial U}{\partial q_{0,y}} & \frac{\partial U}{\partial q_{0,z}} \\ \vdots & \frac{\partial U}{\partial q_{i,w}} & \vdots \\ \frac{\partial U}{\partial q_{n,x}} & \frac{\partial U}{\partial q_{n,y}} & \frac{\partial U}{\partial q_{n,z}} \end{bmatrix} = \begin{bmatrix} \vec{\mathcal{F}}_0 \\ \vdots \\ \vec{\mathcal{F}}_i \\ \vdots \\ \vec{\mathcal{F}}_n \end{bmatrix} \quad (2.15)$$

106 where $\frac{\partial}{\partial q_{i,w}}$ is the derivative with respect to q where w denotes direction of the deriva-
 107 tive (x , y , or z), n is the number of atoms and U is the potential which depends on
 108 q , and \vec{F}_i is the "force" on the i th atom.

109 **No-U-Turn-Sampling**

110 **Grand Canonical Ensemble**

111 **Ensemble description**

112 In the Grand Canonical Ensemble (GCE) two sets of variables are allowed to change,
 113 the atomic positions and the total number of atoms and their associated identities.
 114 These two variables are controlled by temperature and chemical potential. The par-
 115 tition function is

$$\Xi = e^{-\beta(\mathcal{H}+\mu)} \quad (2.16)$$

116 This is translated into a Monte Carlo system, producing Grand Canonical Monte
 117 Carlo (GCMC).

118 **Grand Canonical Monte Carlo**

119 While the probabilities for atomic motion are the same as in the Canonical Ensemble,
 120 the addition or removal of an atom have their own probabilities. For the addition of
 121 an atom the probability is formally:

$$\min[1, \frac{V}{(N+1)\Lambda(T)^3} e^{-\beta\Delta U + \beta\mu}] \quad (2.17)$$

122 Similarly the removal of an atom has the probability:

$$\min[1, \frac{(N)\Lambda(T)^3}{V} e^{-\beta\Delta U - \beta\mu}] \quad (2.18)$$

123 However, both of these equations depend of the overall simulation volume and the
 124 thermal wavelength, which is undesirable as these are not really properties that we

125 are of interest to these simulations. Thus, we roll them into the definition of the
126 chemical potential, essentially setting the base chemical potential to counteract these
127 effects. This makes certain that our simulation does not change if we change the
128 overall cell volume. A GCMC move consists of creating a new atomic configuration,
129 where an atom has been added or removed, and checking the above criteria. However,
130 previous results have shown that this method is computationally expensive in dense
131 liquids, and exceedingly expensive in solid materials. The long simulation times
132 are due to the random nature of the atomic additions or removals which produce:
133 over-tightly packed atoms, atoms in the middle of nowhere, or unphysical vacancies.
134 These configurations are rejected by the GCMC criteria but their probability of being
135 sampled is much higher than configurations which are lower in energy, since the
136 number of incorrect ways to add/remove atoms is much larger than the correct ways.
137 Thus we have implemented methods for biasing the atomic addition positions and
138 the atomic removals toward configurations which are more likely to be accepted.

139 GCMC biasing

140 The first method is to remove some of the excess options from the probability pool.
141 Initially the insertion positions are calculated at random using a random number gen-
142 erator and scaled to the size of the simulation cell. This produces probabilities which
143 have floating point level precision, which is effectively infinite. While this produces
144 a potentially infinite number of ways to create energetically favorable configurations,
145 the infinite ways to produce bad configurations is much larger. Thus we can limit this
146 by moving to voxels. In this case atoms are added to the center of voxels which have
147 a pre-set resolution, limiting our total number of valid addition points. While this
148 could produce some problems with ergodicity, we avoid this by allowing the atoms to
149 translate throughout the system. Each voxel has a probability of being tried:

$$P_{i,j,k} = \frac{xyz}{abc} \quad (2.19)$$

150 where x, y, z and a, b, c are the resolutions and cell side lengths in the cardinal di-
151 rections, respectively. While this does help to limit the total probability space it
152 does not tell us which voxels are likely to lead to better configurations, leading to
153 many rejected atomic additions. To combat this issue we can weigh the individual
154 voxels, giving more probability to voxels which show promise and less to those with
155 less likelihood to be accepted.

156 The approach most likely to yield success would be to measure the change in
157 potential energy associated with the addition of an atom at the center of the voxel
158 where the probability of a voxel to be tried is:

$$P_{i,j,k} = \frac{e^{\beta\Delta U_{i,j,k}}}{\sum_{i,j,k} e^{\beta\Delta U_{i,j,k}}} \quad (2.20)$$

159 where $\Delta U_{i,j,k}$ is the change in energy. However, calculating $\Delta U_{i,j,k}$ can be particu-
160 larly expensive, especially when calculating scattering from atomic positions. The
161 computational expense can be mitigated by using a cheaper potential, if only for the
162 evaluation of the voxel energy, as previously shown. Similar to previous work we can
163 use the Lennard Jones potential to approximate the addition potential.

164

CHAPTER 3

165

ATOMIC PAIR DISTRIBUTION FUNCTION:

166

THEORY AND COMPUTATION

167 3.1 THEORY

168 To properly understand the PDF and its limitations we need to derive its mathemat-
169 ics. The following derivation has been performed numerous times but most recently
170 and completely by Farrow and Billinge, it is reproduced here for clarity and com-
171 pleteness.

172 **Derivation**

173 **Analytical Gradients**

174 Many optimization algorithms and simulations methodologies, including HMC, re-
175 quire not only the potential energy of a given configuration but also the forces acting
176 on that configuration. These forces are described by the gradient of potential energy
177 of the system which in turn requires the gradient of the PDF. As previously shown the
178 PDF is the Fourier Transform of the Debye equation. Since the Fourier Transform is
179 expressed as an integral we can exchange the order of the gradient and the integral,
180 allowing us to calculate the analytical gradient of the Debye equation and FFT the
181 resulting function. The Debye equation, with a Debye-Waller vibrational correction
182 is

$$F(Q) = \frac{1}{N\langle f \rangle^2} \sum_{j \neq i} f_i^*(Q) f_j(Q) \exp(-\frac{1}{2}\sigma_{ij}^2 Q^2) \frac{\sin(Qr_{ij})}{r_{ij}} \quad (3.1)$$

183 where

$$\sigma_{ij}^2 = (\vec{u}_{ij} * \hat{d}_{ij})^2 \quad (3.2)$$

$$\vec{u}_{ij} = \vec{u}_i - \vec{u}_j \quad (3.3)$$

$$\hat{d}_{ij} = \frac{\vec{d}_{ij}}{r_{ij}} \quad (3.4)$$

$$r_{ij} = \|\vec{d}_{ij}\| \quad (3.5)$$

$$\vec{d}_{ij} = \begin{bmatrix} q_{ix} - q_{jx} \\ q_{iy} - q_{jy} \\ q_{iz} - q_{jz} \end{bmatrix} \quad (3.6)$$

184 where Q is the scatter vector, f_i is atomic scattering factor of the i th atom, and r_{ij}
 185 is the distance between atoms i and j and has q dependence. For simplicities sake
 186 we will break up $F(Q)$ so that

$$F(Q) = \alpha \sum_{j \neq i} \beta_{ij} \tau_{ij} \Omega_{ij} \quad (3.7)$$

187 where

$$\alpha = \frac{1}{N\langle f \rangle^2} \quad (3.8)$$

$$\beta_{ij} = f_i^*(Q) f_j(Q) \quad (3.9)$$

$$\tau_{ij} = \exp(-\frac{1}{2} \sigma_{ij}^2 Q^2) \quad (3.10)$$

$$\Omega_{ij} = \frac{\sin(Qr_{ij})}{r_{ij}} \quad (3.11)$$

188 The derivatives are as follows:

$$\frac{\partial}{\partial q_{i,w}} F(Q) = \alpha \sum_j \beta_{ij} \left(\frac{\partial \tau_{ij}}{\partial q_{i,w}} \Omega_{ij} + \tau_{ij} \frac{\partial \Omega_{ij}}{\partial q_{i,w}} \right) \quad (3.12)$$

189 where

$$\frac{\partial \Omega_{ij}}{\partial q_{i,w}} = \frac{Q \cos(Qr_{ij}) - \Omega_{ij}}{r_{ij}^2} (q_{i,w} - q_{j,w}) \quad (3.13)$$

$$\frac{\partial \tau_{ij}}{\partial q_{i,w}} = \frac{\sigma_{ij} Q^2 \tau_{ij}}{r_{ij}^3} ((q_{i,w} - q_{j,w}) \sigma_{ij} - (u_{i,w} - u_{j,w}) r_{ij}^2) \quad (3.14)$$

190 Since \vec{u}_{ij} is a variable as well, we need the derivative with respect to it as well.

191 Thus

$$\frac{\partial}{\partial u_{i,w}} F(Q) = \alpha \sum_j \beta_{ij} \frac{\partial \tau_{ij}}{\partial u_{i,w}} \Omega_{ij} \quad (3.15)$$

$$\frac{\partial \tau_{ij}}{\partial u_{i,w}} = -\frac{\sigma_{ij} Q^2 \tau_{ij}}{r_{ij}} (q_{i,w} - q_{j,w}) \quad (3.16)$$

192 **Without ADPs**

193 Without ADPs the equations simplify down to

$$F(Q) = \frac{1}{N \langle f \rangle^2} \sum_{j \neq i} f_i^*(Q) f_j(Q) \frac{\sin(Qr_{ij})}{r_{ij}} \quad (3.17)$$

194 and

$$\frac{\partial}{\partial q_{i,w}} F(Q) = \alpha \sum_j \beta_{ij} \frac{\partial \Omega_{ij}}{\partial q_{i,w}} \quad (3.18)$$

195 use of these equations, when ADPs are not appropriate (like at cryogenic tempera-
196 tures), greatly speeds up the computaiton.

197 **3.2 COMPUTATION**

198 Simply deriving the equations for the PDF is not enough. The many body nature of
199 the PDF equation make analytical solution of the structure from the PDF impossible.
200 Thus, the PDF must be computed from a structural candidates and compared against
201 experimental results to evaluate the reliability of the model.

202 **HPC and GPUs**

203 To properly solve the structure of materials the PDF will need to be computed many
204 times and checked against experimental results. This requires computation of the
205 PDF, potentialy over many atoms. Calculating these PDFs requires a fast, highly
206 parallized, computational framework.

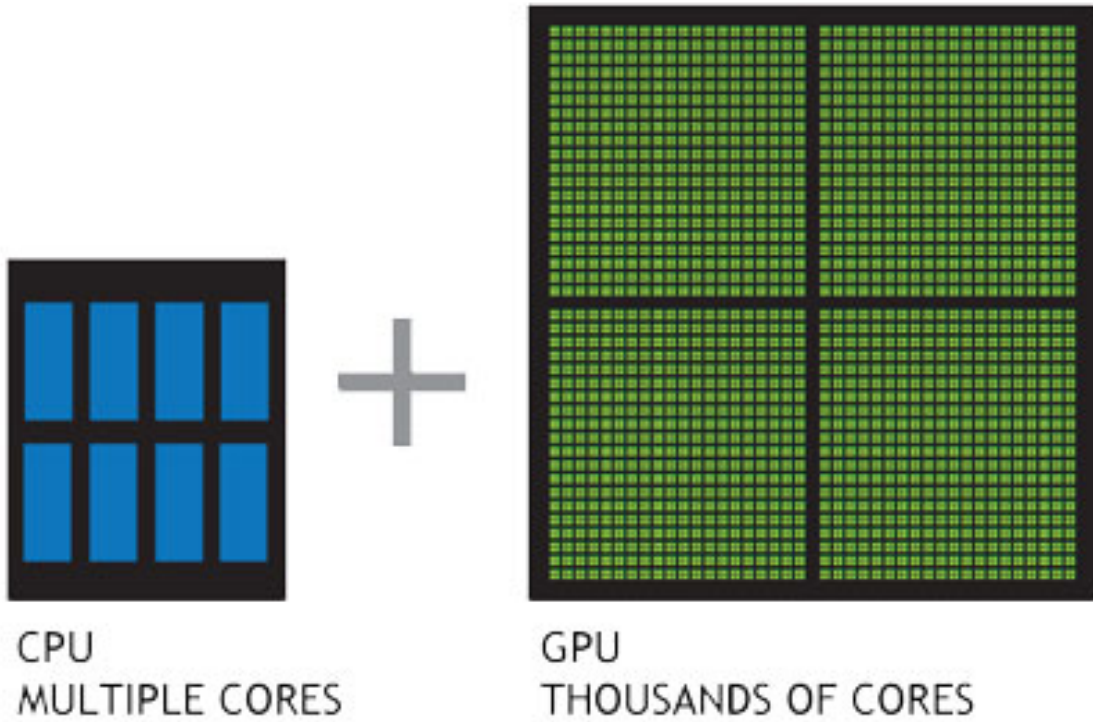


Figure 3.1: Comparison of the CPU and GPU chip architectures

207 GPUs and Parallelization

208 Computing the PDF is an embarrassingly parallel problem. The basic procedure is
 209 to calculate the reduced structure factor $F(Q)$ for each atom pair and momentum
 210 transfer vector, sum over all the atom pairs, and Fourier transform the structure to
 211 the PDF. The first part of this procedure is perfectly parallelizable, as each atom pair is
 212 separate from the others. The summation over all the atomic reduced structure factors
 213 can be parallelized via distributed summing. Lastly the FFT can be parallelized using
 214 existing parallel FFT algorithms.

215 GPUs are particularly well suited to the task of computing PDFs. GPU chip
 216 architecture is designed to perform many tasks simultaneously by having potentially
 217 thousands of cores.

218 Map from ij space to k space

219 The above equations, although formally correct, are very ineffiecent. $F(Q)$ and its
 220 gradient are indexed over all the atoms twice, however there are symmetries that
 221 allow us to only compute over the atom pairs esentially mapping from an $n \times n$ space,
 222 ij space, to a $\frac{n(n-1)}{2}$ space, k space. For $F(Q)$ we apply the following mapping where

$$\begin{array}{ccccc} & & \psi & & \\ E & \xrightarrow{\quad} & E' & \xrightarrow{\Sigma} & Z \\ \phi \downarrow & & & \nearrow \Sigma' & \\ B & \xrightarrow{\quad} & B' & & \end{array}$$

223

224 E denotes the atomic coordinates in ij space, E' denotes $F(Q)$ before the summation
 225 in ij space, B denotes the atomic pairs in k space, B' denotes $F(Q)$ in k space, and
 226 Z denotes the final summed $F(Q)$. For the operators, ϕ denotes the mapping from
 227 ij space to k space $k = j + i * \frac{i-1}{2}$, ψ and ψ' denote the $F(Q)$ operation in ij and k
 space, respectivly. Σ denotes the sum over all the atoms.

228 To properly define Σ' we must establish whether $F(Q)$ is an even function. We
 229 can accomplish this by examining each of the portions of $F(Q)$, $\alpha, \beta, \tau, \Omega$. Ω is even,
 230 since r_{ij} is the interatomic distance, which is the same despite a flip of indicies, Q
 231 does not depend on the atomic indicies, and since Qr_{ij} is even so is $\sin Qr_{ij}$. Thus,
 232 Ω is even. Providing similar analysis to τ we can see that while \vec{u}_{ij} is odd, so is
 233 the unit displacement vector between the two atoms, thus the two odds cancel out.
 234 Intuitivly this makes sense, since the $F(Q)$ equation is fundamentally interested in the
 235 interatomic distances which is even. Thus, switching atom indicies does not change
 236 $F(Q)$. Due to the even nature of the $F(Q)$ operator the Σ' operator sums over all the
 237 atom pairs, and multiplies by two to reflect the double counting of the Σ operator.

238 For the gradient a similar mapping is used:

239 In this mapping, however, we use the $\tilde{\phi}\Sigma$ operator. This operator simultaniously

$$\begin{array}{ccccc}
& & \psi & & \Sigma \\
E & \xrightarrow{\quad} & E' & \xrightarrow{\quad} & Z \\
\phi \downarrow & & & \nearrow \tilde{\phi}\Sigma & \\
B & \xrightarrow{\quad} & B' & &
\end{array}$$

240 performs a reverse mapping from k to ij space, and a summation with the correct
 241 symmetry. In this case the ψ and ψ' operators, which denote the $\vec{\nabla}F(Q)$ operator
 242 in ij and k space, are antisymmetric. Intuitivly this makes sense as an extension of
 243 Newton's Second Law, since each particle's interation is felt oppositely by its partner.

244 Periodic Boundary Conditions

245 Periodic boundary conditions can be helpful when simulating extended solids or large
 246 nanoparticles. In this case all the non-crystallinity is contained within the simulation
 247 box and the box is repeated to create the longer distance peaks observed in the PDF.
 248 To perform this we can break up the Debye equation into two main parts, the part
 249 that describes the interatomic distances within the simulation box and those between
 250 boxes. Neglecting the thermal motion portion:

$$F(Q) = \frac{1}{N\langle f \rangle^2} \left(\sum_{j \neq i} f_i^*(Q) f_j(Q) \frac{\sin(Qr_{ij})}{r_{ij}} + \sum_{i,j} f_i^*(Q) f_j(Q) \frac{\sin(QR_{ij})}{R_{ij}} \right) \quad (3.19)$$

251 where

$$R = |\vec{r} + \vec{u}| \quad (3.20)$$

$$\vec{u} = \gamma_1 * \vec{a} + \gamma_2 * \vec{b} + \gamma_3 * \vec{c} \quad (3.21)$$

252 3.3 EXPERIMENT

253 PDF experiments are generally performed at synchrotron light sources, as only these
 254 sources can provide the need flux, energy, and high momentum transfer vectors needed
 255 to obtain relyable PDFs.

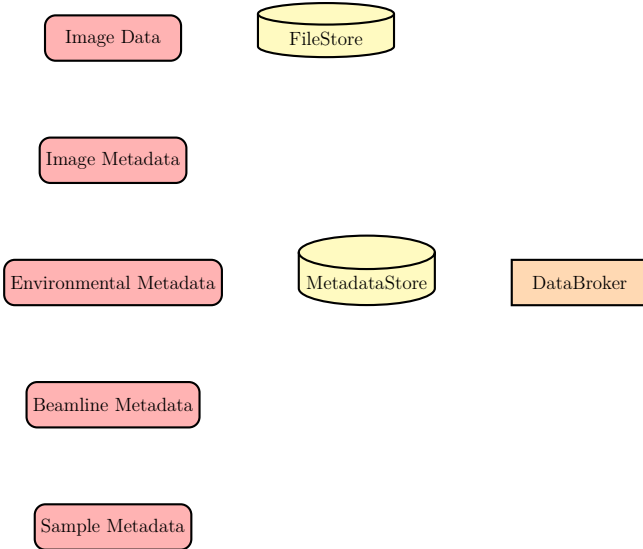


Figure 3.2: Database Loading Workflow. Data is loaded from various sources, including images and text files, into the FileStore and MetadataStore databases. Data is then retrieved from the databases using the databroker.

256 3.4 DATA PROCESSING WORKFLOW

257 Processing the raw pixel intensities to the PDF is very important as we are extracting
 258 most of our interesting information out of very high Q data. This data relies on good
 259 statistics and sound background subtraction. Talk about papers from Billinge Group
 260 with thin film PDF and dilute NP solutions. Diagram of the overall data processing
 261 workflow. Discuss the NSLS-II data stack.

262 **MetadataStore Side Loading**

263 Design of sidewinder-spec for loading the data into metadatastore. Most of the design
 264 considerations went into the loaders, which are different for each experiment.

265 **Detector Q resolution**

266 To properly azimuthally integrate the images taken from the detector the Q resolution
 267 of the pixels must be calculated. Integrating using even bins will cause pixels which

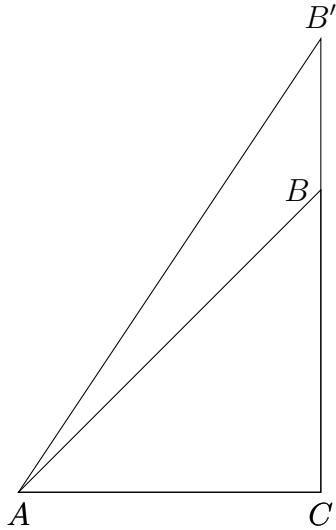


Figure 3.3: Scattering onto a flat detector

are not on the same ring to be binned together, causing the incorrect value of $I(Q)$ to be obtained and a larger standard deviation in the integrated data. To properly calculate the Q resolution the resolution of each of the pixels in 2θ must be calculated. Figure 3.3 shows the scattering of x-rays onto a flat image plate detector. In this diagram the bottom of the n th pixel is B while the top is B' . The resolution of this pixel in 2θ is $\angle BAC - \angle B'AC$. Thus the resolution, calculated from the distances is

$$\Delta 2\theta = \arctan \frac{b}{d} - \arctan \frac{t}{d} \quad (3.22)$$

where d is the sample to detector distance, b is the distance to the bottom of a pixel, and t is the distance to the top of that pixel. Note that these distances need to have been corrected for detector tilt and rotation. Thus the resolution of a pixel in Q is

$$\Delta Q = \frac{4\pi(\sin \arctan \frac{b}{d} - \sin \arctan \frac{t}{d})}{\lambda} \quad (3.23)$$

where λ is the x-ray wavelength.

For a Perkin Elmer image plate, like the one used at the NSLS-II's XPD and the APS's 11-ID-B, the resolution function is shown in 3.4. For the same detector the number of pixels per Q is shown in 3.5

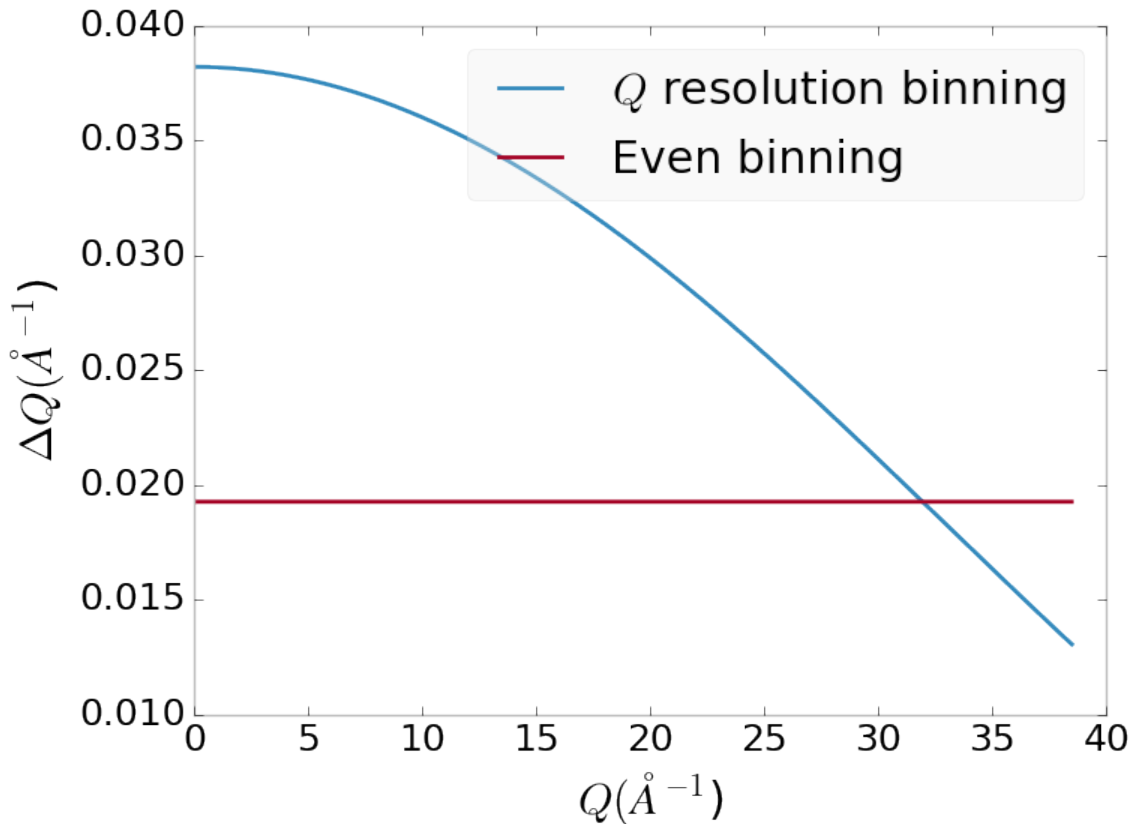


Figure 3.4: Q resolution as a function of Q .

281 Automated Mask Generation

282 Introduction

283 Detector masking is an important part of any x-ray scattering workflow as dead/hot
 284 pixels, streak errors, and beamstop associated features can be averaged into the data
 285 changing the signal and its statistical significance. While some features, like the
 286 beamstop holder, can be easily observed and masked by hand other are much more
 287 difficult to observe even on large computer monitors. Additionally, while dead/hot
 288 pixels and streaks are usually static the hot pixels associated with textured or sin-
 289 gle crystal scattering or cosmic rays are not. Thus, coming up with an automated
 290 method for finding such erroneous pixels is important, especially as high flux diffrac-
 291 tion beamlines can generate data very quickly.

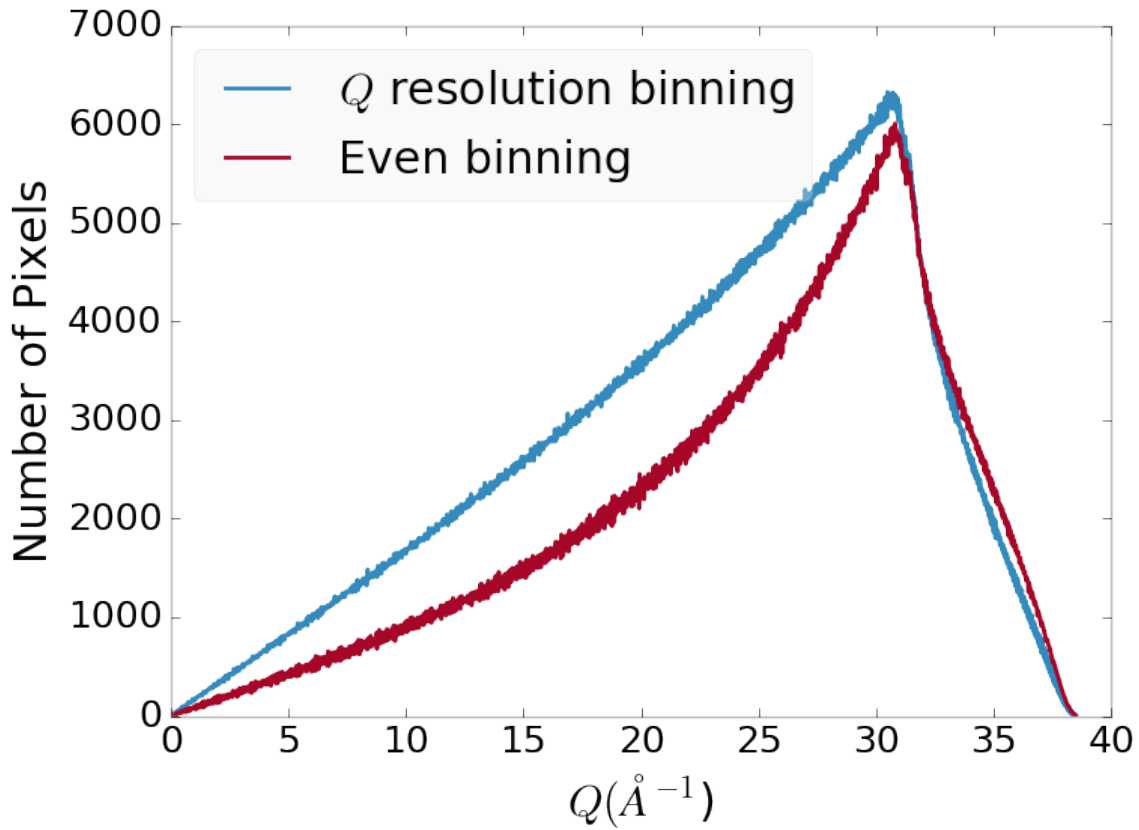


Figure 3.5: Number of pixels as a function of Q , binned at the Q resolution of the detector.

292 While this problem can be quite complex in the most general case, we can use the
 293 annular symmetry of the powder scattering pattern to our advantage, by comparing
 294 a pixel against pixels in the same ring. Since non-textured powder scattering should
 295 produce the same pixel intensity for a given ring we can mask any pixels which are α
 296 standard deviations away from the mean. This method relies on the aforementioned
 297 pixel binning algorithm, as using miss sized bins will cause some pixels which should
 298 be in separate rings to be put together, and others which should be in the same ring
 299 to be separated. In that case the masking algorithm will overestimate the number of
 300 pixels to be masked due to the additional statistical variation in the sample.

301 **Algorithm Design**

302 The masking algorithm procedure takes in the image and a description of the pixel
303 positions in either distance from the point of incidence or in Q . The image is then
304 integrated twice, producing both the mean $I(Q)$ and the standard deviation of each
305 $I(Q)$ ring. The mask is created by comparing the pixel values against each ring's
306 standard deviation and threshold α . Note that the threshold can be a function of
307 distance from the point of incidence or Q .

308 **Test Cases**

309 To study the effectiveness of the masking we ran the algorithm against both simulated
310 experimental data. In the case of the simulated data four systems were created: 1)
311 dead/hot pixels with varying numbers of defective pixels, 2) beamstop holder with
312 varying beamstop holder transmittance, 3) rotated beamstop holder with varying
313 beamstop holder transmittance, and 4) beamstop holder with dead/hot pixels. The
314 base scattering was produced by

$$I = 100 \cos(50r)^2 + 150 \quad (3.24)$$

315 where r is a pixel's distance from the beam point of incidence. The positions of
316 the dead/hot pixels were chosen at random as was the dead or hot nature of the
317 defect. Dead pixels had values from 0 to 10, while hot pixels had values from 200
318 to 255. The beamstop was positioned at the vertical center of the detector with an
319 initial width of 60 pixels and final width of 120 pixels. The height of the beamstop
320 was 1024 pixels. The beamstop was calculated to attenuate the x-ray scattering
321 signal at various transmittance, as various beamstop holder materials have different
322 transmittance. Two versions of the masking algorithm were run for each test case, one
323 using the standard even bin sizes for the integration step, and one where the bin sizes
324 are tuned to the pixel Q resolution as discussed in 3.4.

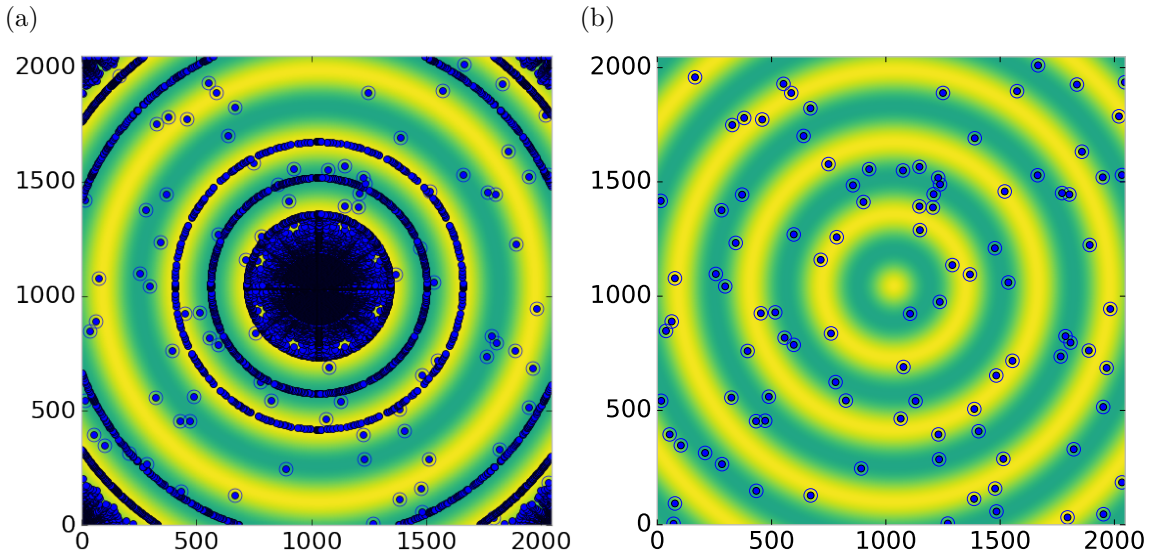


Figure 3.6: Generated dead/hot pixel masks for a detector with 100 bad pixels. a) the standard even bin mask and b) the Q resolution binned mask. The bad pixels are noted with open circles, masked pixels are noted with closed circles.

325 Results and Discussion

326 Figures 3.6-3.13 show the results of the masking algorithm on simulated images. The
 327 dead/hot pixel masking shows the importance of using the Q resolution based bin sizes
 328 as the even bin based mask have a tendency to over mask the image, removing pixels
 329 which contain valuable signal. This overmasking is caused by pixels being improperly
 330 associated with one another by the even bins. Figure 3.6 indicates that the masking
 331 algorithm, with the proper binning, masks the image perfectly, with no missed bad
 332 pixels or good pixels masked. This is not the case in figures 3.7 - 3.9 as we can see
 333 pixels which should have been masked but were not. Despite these missed pixels no
 334 pixels were improperly masked in any of the well binned images. These test cases
 335 are actually more difficult than experimental data, as the dynamic range of most
 336 detector causes the dead/hot pixels and single crystal/textured peaks to be orders of
 337 magnitude away from the desired signal.

338 The beamstop holder masks shown in figures 3.10 - 3.13, which were all run with

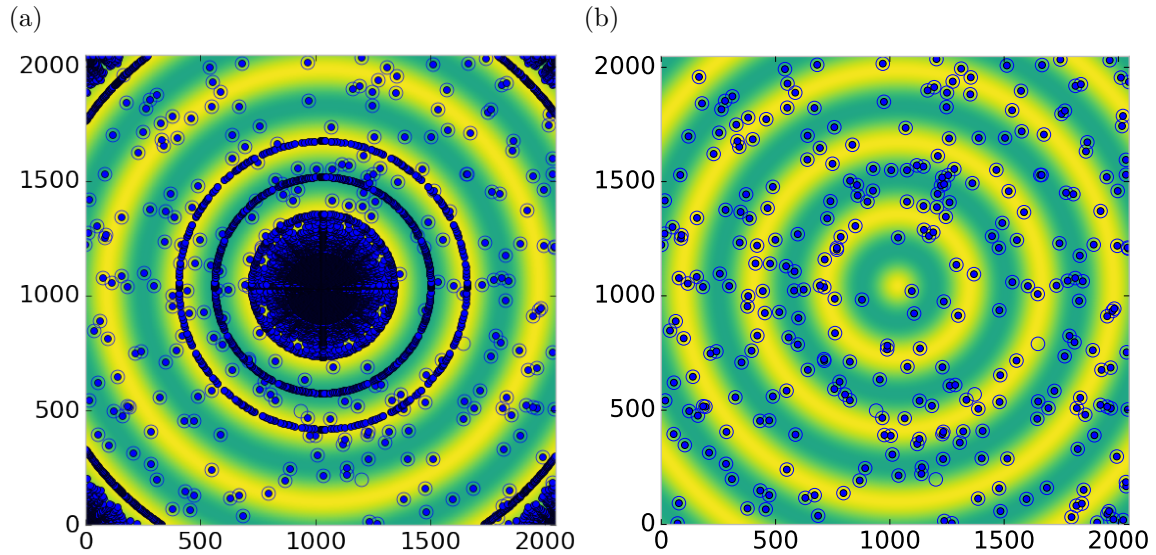


Figure 3.7: Generated dead/hot pixel masks for a detector with 300 bad pixels. a) the standard even bin mask and b) the Q resolution binned mask. The bad pixels are noted with open circles, masked pixels are noted with closed circles.

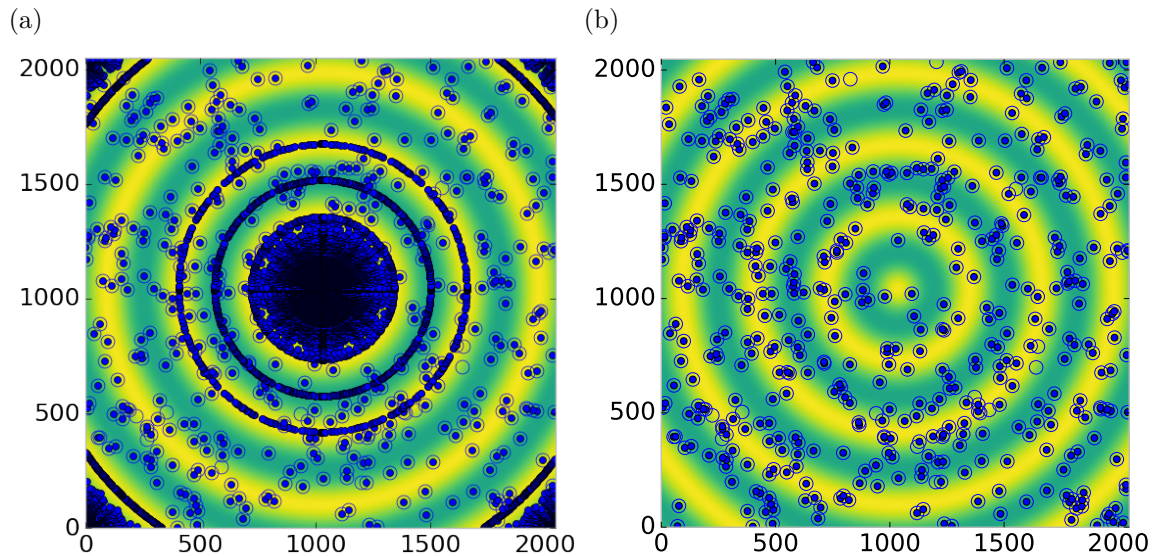


Figure 3.8: Generated dead/hot pixel masks for a detector with 500 bad pixels. a) the standard even bin mask and b) the Q resolution binned mask. The bad pixels are noted with open circles, masked pixels are noted with closed circles.

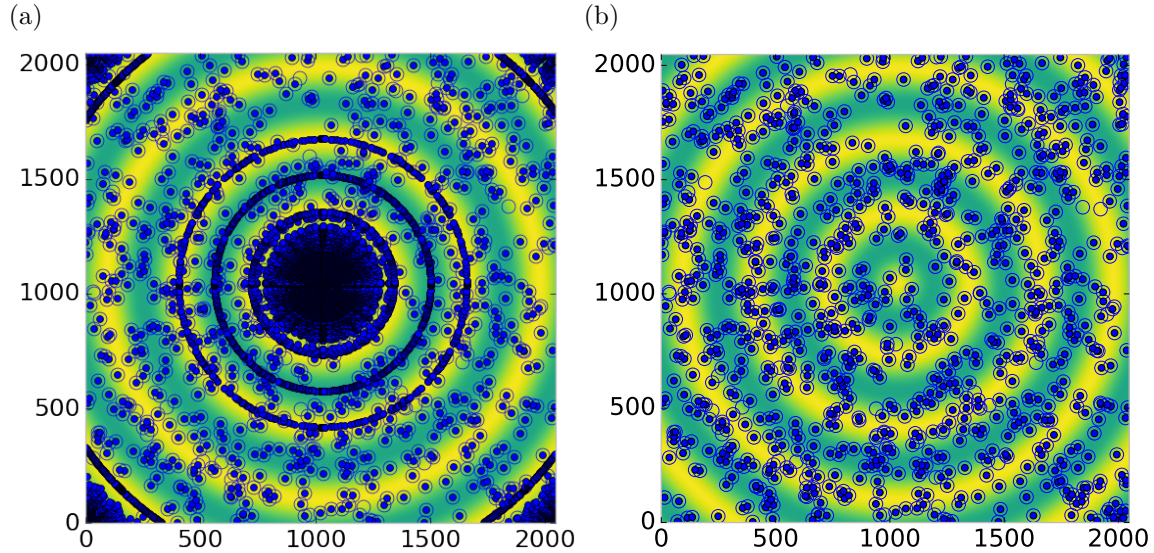


Figure 3.9: Generated dead/hot pixel masks for a detector with 1000 bad pixels. a) the standard even bin mask and b) the Q resolution binned mask. The bad pixels are noted with open circles, masked pixels are noted with closed circles.

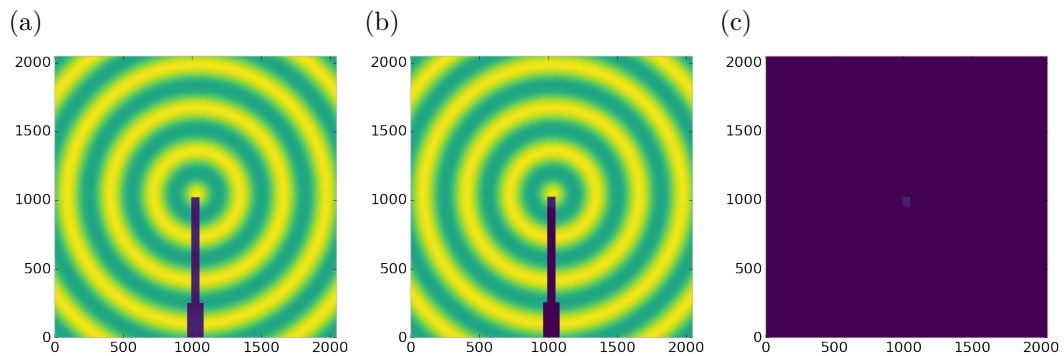


Figure 3.10: Generated beamstop holder masks for a beamstop holder with 10% transmittance. a) the raw image, b) the masked image, c) and the missed pixels

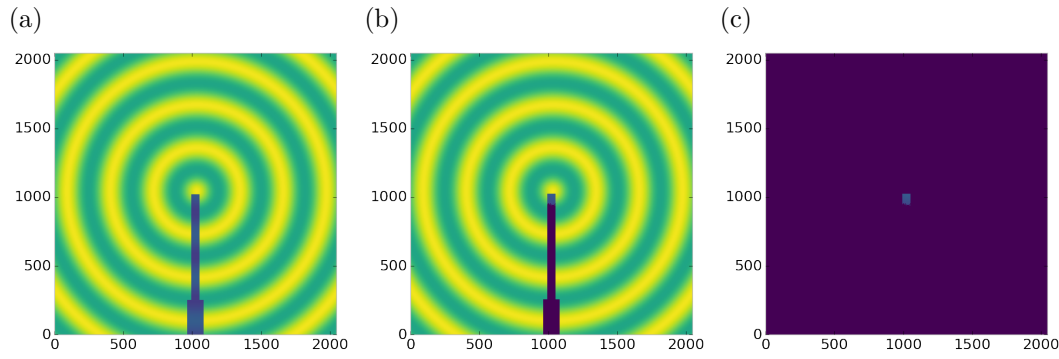


Figure 3.11: Generated beamstop holder masks for a beamstop holder with 30% transmittance. a) the raw image, b) the masked image, c) and the missed pixels

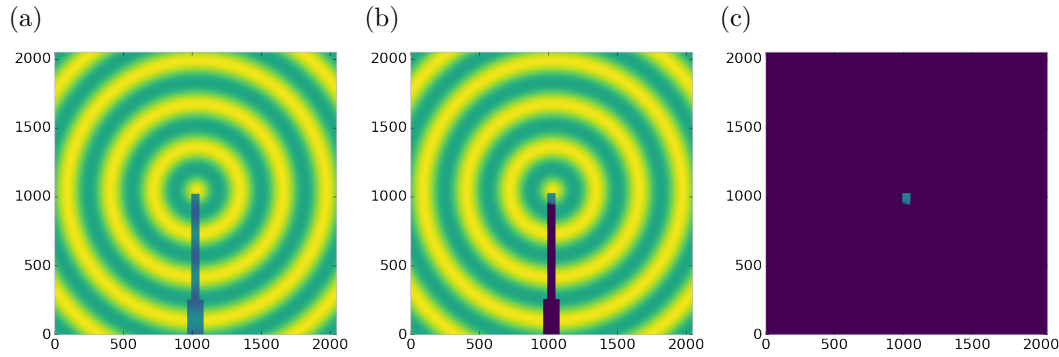


Figure 3.12: Generated beamstop holder masks for a beamstop holder with 50% transmittance. a) the raw image, b) the masked image, c) and the missed pixels

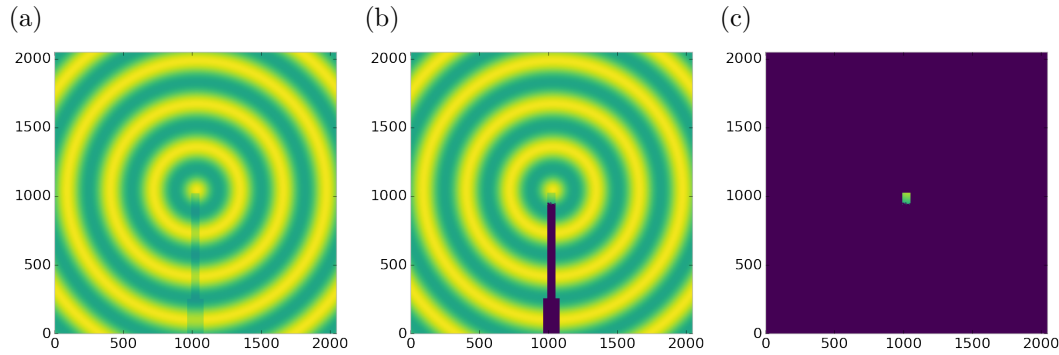


Figure 3.13: Generated beamstop holder masks for a beamstop holder with 90% transmittance. a) the raw image, b) the masked image, c) and the missed pixels

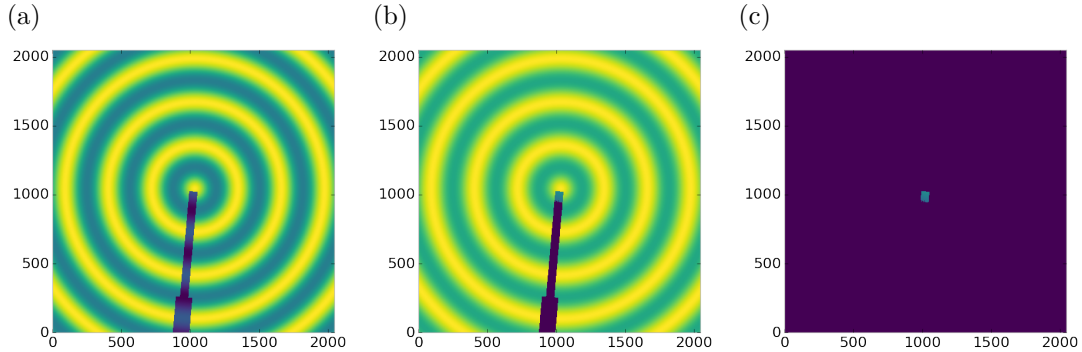


Figure 3.14: Generated beamstop holder masks which is rotated away from verticle

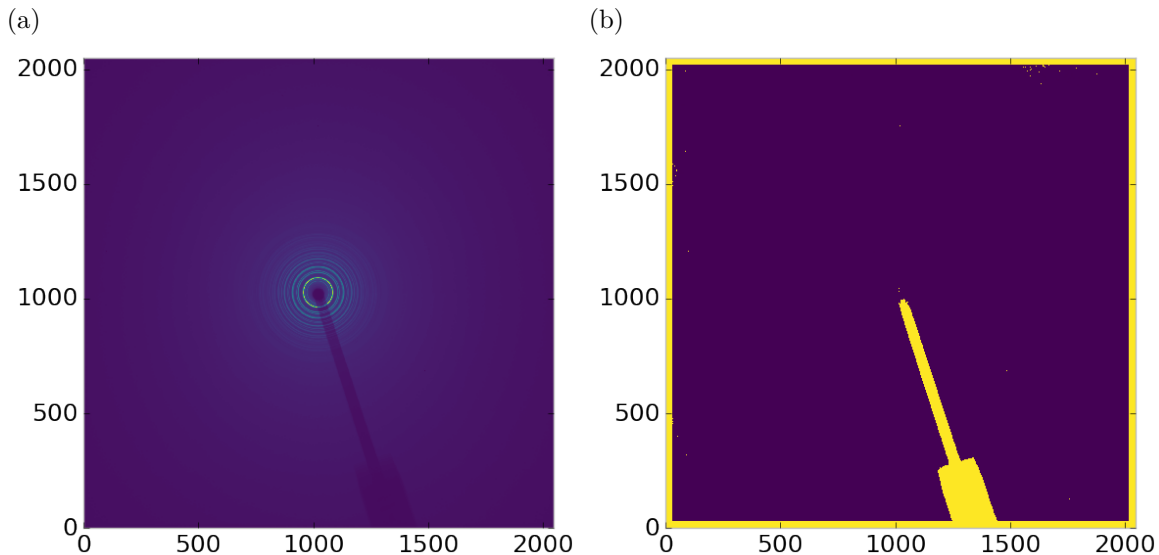


Figure 3.15: Masked experimental data. a) the raw image, b) the mask

339 the Q resolution binning show similar results across the transmittance range, missing
 340 only a small part of the beamstop holder near the point of incidence. Near this point
 341 the beamstop holder becomes a statisticly significant part of the total number of
 342 pixels in a given ring, thus it can not be masked out using a statistical search of the
 343 rings. For most PDF and XRD studies this small area can be masked automaticly
 344 by masking all the pixels who's distance from the point of incidence is smaller than a
 345 given radius r , or can be negelected outright as the area is not used in the analysis or
 346 refinement. Similar results were produced for beamstop holders which were rotated
 347 away from the vericle position, as shown in figure 3.14

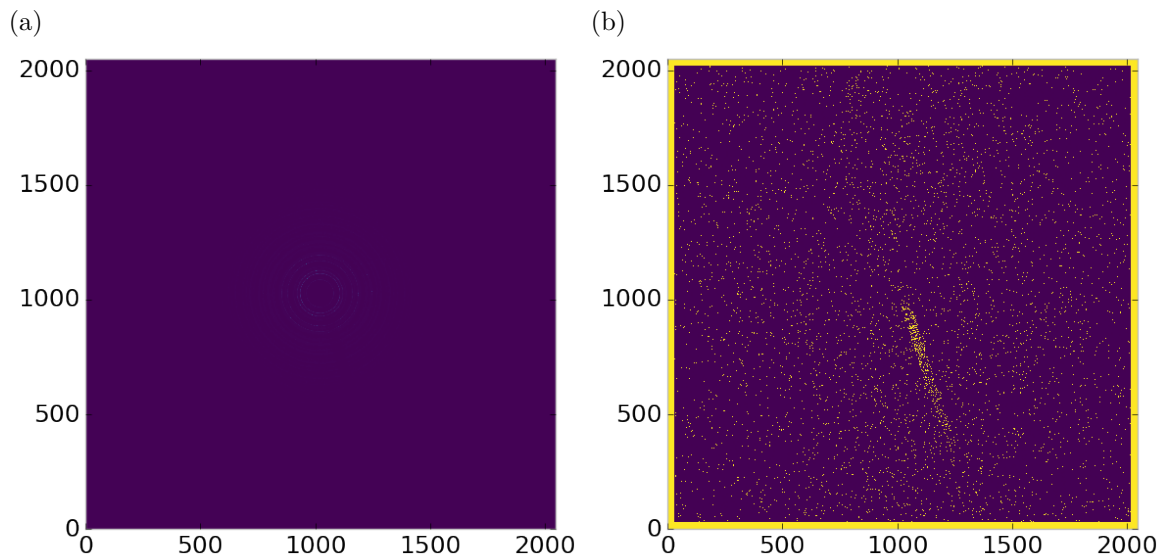


Figure 3.16: Masked experimental data with Pt single crystal signal. a) the raw image, b) the mask

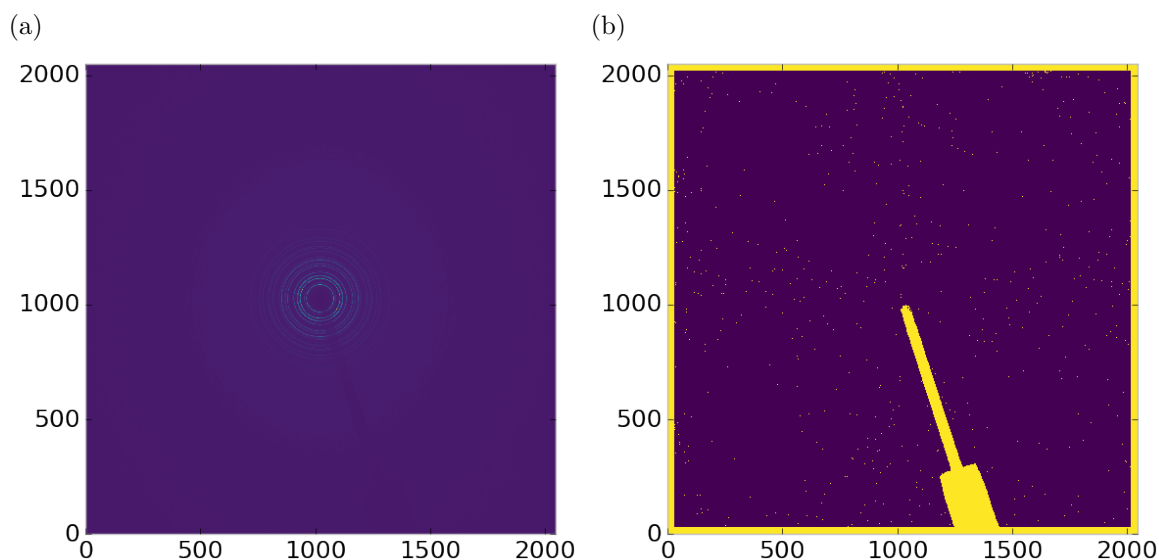


Figure 3.17: Masked experimental data with Pt single crystal signal using figure's 3.15 as a starting mask. a) the raw image, b) the mask

348 Working with actual experimental data, obtained at the Advanced Photon Source
349 beamline 11-ID-B, shows the difficulty of masking images which have low phonon
350 counts. While the masking of experimental data taken with longer exposures, con-
351 sisting of 250 .2 second shots, shown in figure 3.15 provides very sharp edges to the
352 beamstop holder, and very little extra masking beyond the occasional dead pixel, this
353 is not the case for the single crystal data. The single crystal data is more problem-
354 atic because of its short exposure time and low flux, with 500 frame at a .1 second
355 exposure and having shrunk the beam size. The low flux is to prevent the very strong
356 single crystal peaks from damaging the detector. However, this causes the image to
357 be less statistically viable than ideal, causing problems with the mask as seen in figure
358 3.16. This can be alleviated to some degree by using the previously generated mask
359 as a starting mask for the single crystal image, as shown in 3.17. While the masking
360 algorithm still produces many diffuse masked pixels, they are far fewer, this may
361 be due to the removal of the beamstop which could have contributed to the large
362 standard deviation in figure 3.16.

363 **Conclusions**

364 In this section the masking algorithm, which relies on both Q resolution based binning
365 and a statistical approach to azimuthal symmetry, was developed. The focus of
366 this algorithm was to remove many unwanted detector features associated with pixel
367 defect, beamstop holder associated scattering attenuation, and single crystal/texture
368 peaks. Simulated data was used to evaluate the beamstop holder and dead/hot pixel
369 masking capacity, while experimental data was used to check for single crystal and
370 texture based masking. Q resolution based binning was shown to be very important to
371 avoid overmasking. The ability of the mask writer to mask images is somewhat limited
372 by the overall statistical image quality, although some deficiencies can be obtained by
373 using previously generated masks as starting points. This masking algorithm is now

374 in use in the data processing workflow and will be available in scikit-beam soon.

375 Automated Image Azimuthal Integration

376 Using the Q resolution binning and masking developed in sections 3.4 and 3.4 the
377 images can be properly integrated. Generally, images are integrated by taking the
378 mean value of the pixels in a ring. However, other statistical measures of the average
379 value can be used, like the median.

380 Figures 3.18-3.20 show the importance of masking and the choice of average func-
381 tion. All the figures were produced using the same dataset, 50 °C Pr_2NiO_4 taken at
382 the APS’s 11-ID-B on a Perkin Elmer area detector. The automatic masking alpha
383 was 3 standard deviations from the mean. While it is difficult to observe the changes
384 the mask causes in the full $I(Q)$ plot (subfigures a) and b)), the standard deviation
385 plots show the effect of bad pixels on the data (subfigure c)). Subfigure c) for figures
386 3.18-3.20 shows that removal of the beamstop holder lowers the low Q standard de-
387 viation from around .1 to almost .01 out to 15 Å⁻¹. The high Q subfigures d) and f)
388 in figures 3.18-3.20 show the “kink” effect of the detector edge and beamstop holder,
389 where there is a dip in the $I(Q)$ scattering when the rings include the edge of the
390 detector. This effect seems to be due to both errors in the edge pixel intensity and the
391 beamstop holder as masking of the edges only seems to provide only partial removal
392 of the issue. It is important to note that while integration using the mean of the
393 ring has issues with only the edge mask, as evidenced by the change in slope in 3.19
394 d) around 29.5 Å⁻¹, the median integration does not include this error. Ideally the
395 detector would have a normal distribution of pixel intensity for a given ring, which
396 would imply an equivalency between the mean and median $I(Q)$ values. Despite the
397 closeness of the mean and median once the final mask has been created, it seems that
398 the median is more reliable, as it was less effected by the beamstop holder in figure
399 3.19. Thus, for subsequent integrations discussed in this work the median is used to

400 avoid any defective features that the masking algorithm may have missed.

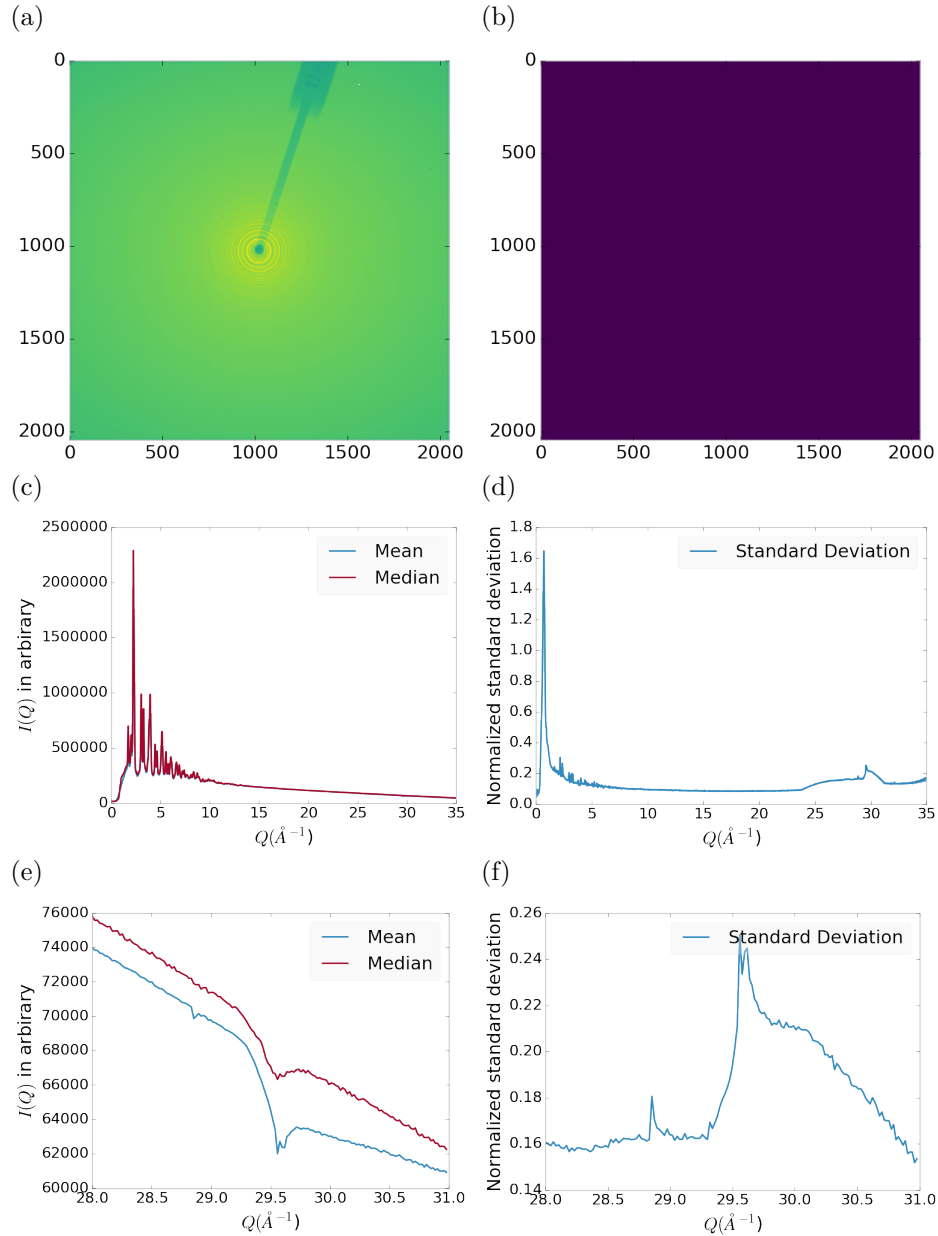


Figure 3.18: Masking, average, and standard deviation of an example x-ray total scattering measurement. This image was produced with no mask. a) the image, b) the mask, c) the mean and median values, d) the standard deviation (normalized to the median), e) a closeup of the 28\AA^{-1} to 31\AA^{-1} Q range for the mean and median, f) 28\AA^{-1} to 31\AA^{-1} Q range for the standard deviation

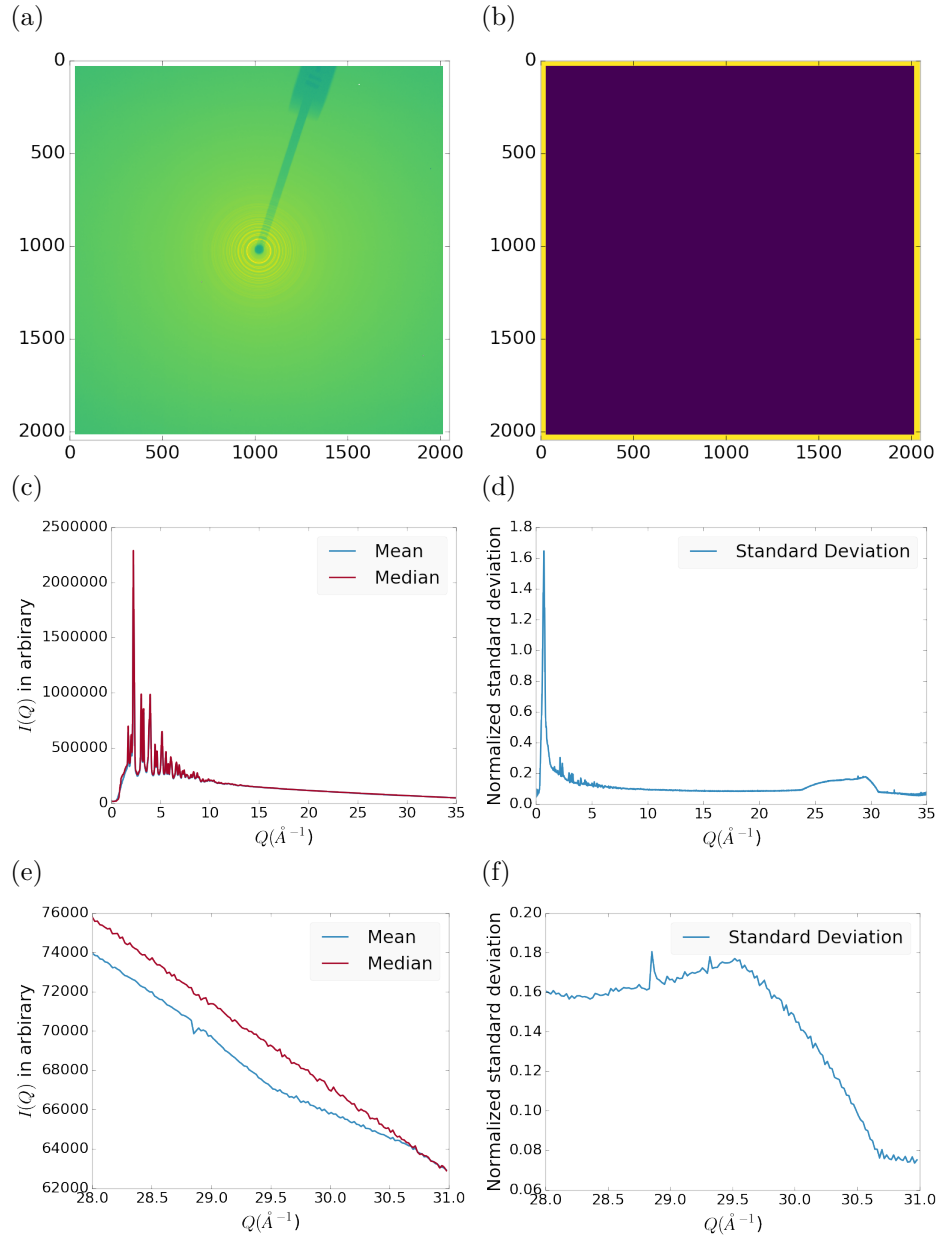


Figure 3.19: Masking, average, and standard deviation of an example x-ray total scattering measurement. This image was produced with only an edge mask. a) the image, b) the mask, c) the mean and median values, d) the standard deviation (normalized to the median), e) a closeup of the 28\AA^{-1} to 31\AA^{-1} Q range for the mean and median, f) 28\AA^{-1} to 31\AA^{-1} Q range for the standard deviation

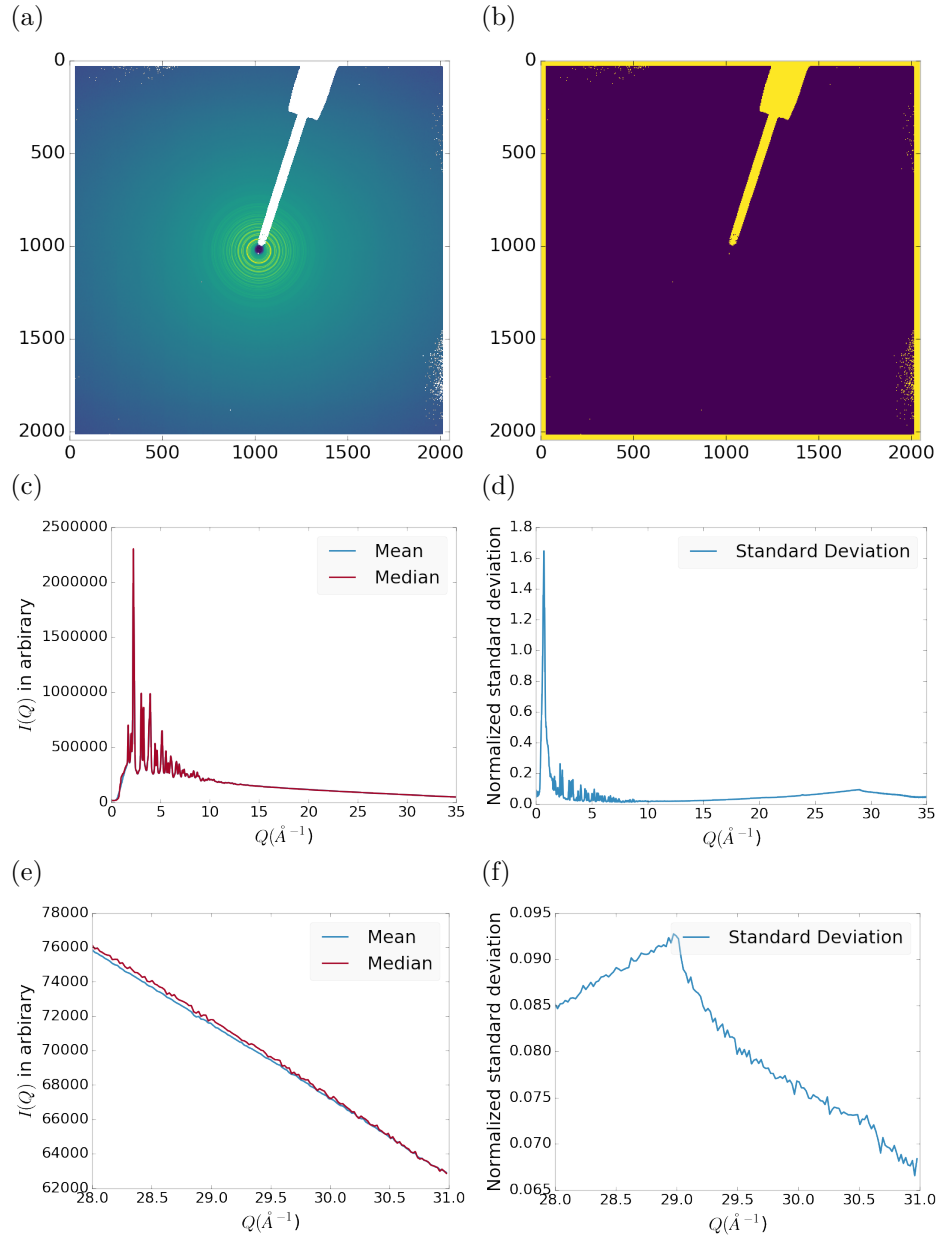


Figure 3.20: Masking, average, and standard deviation of an example x-ray total scattering measurement. This image was produced combining an edge mask and the automatically generated mask. a) the image, b) the mask, c) the mean and median values, d) the standard deviation (normalized to the median), e) a closeup of the 28 \AA^{-1} to 31 \AA^{-1} Q range for the mean and median, f) 28 \AA^{-1} to 31 \AA^{-1} Q range for the standard deviation

401

CHAPTER 4

402

BENCHMARKING

403 4.1 PDF

404 **Au55:** surface relaxed

405 **Au55:** surface disordered

406 **Au55:** amorphous

407 **Au102:** triple phase

408 **FCC**

409 **Marks decahedron**

410 **Au147**

411 4.2 PDF WITH ADPs

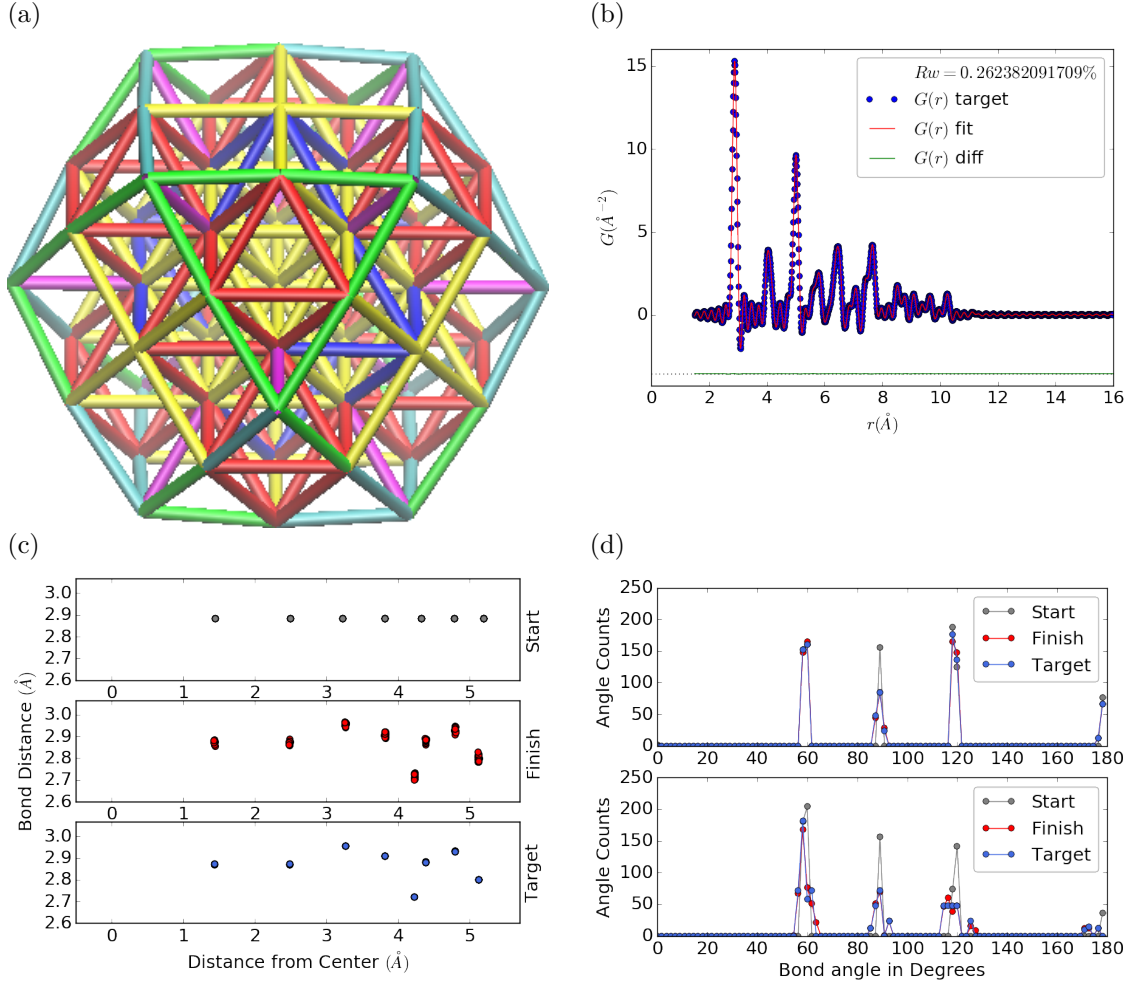


Figure 4.1: Au₅₅ PDF fitting of DFT-optimized c -Au₅₅. a) the final structural solution ($Rw=0.3\%$) with bond lengths color-coded by step of 0.05 \AA , b) the target PDF(blue dots) overlaid with the PDF of the final structure (solid red lines) with the difference in green lines offset below, c) the radial bond distribution, and d) bond angle distribution.

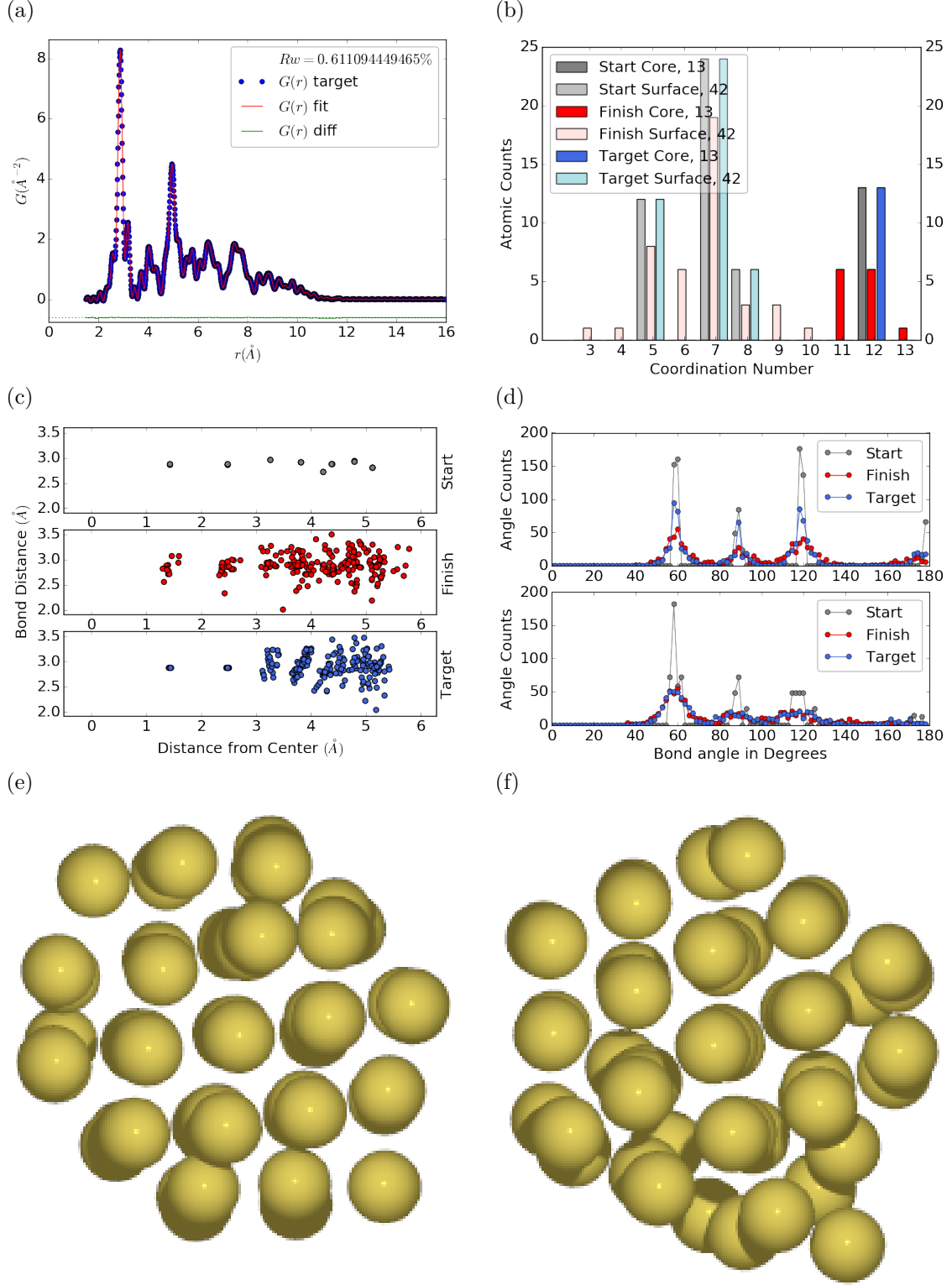


Figure 4.2: Au_{55} PDF fitting of surface-disordered Au_{55} . a) the target structure, b) the final structural solution ($R_w=0.6\%$), c) the comparison of PDFs, d) the CN distribution with the number of atoms in either the core or the surface, e) the radial bond distribution, and f) the bond angle distribution.

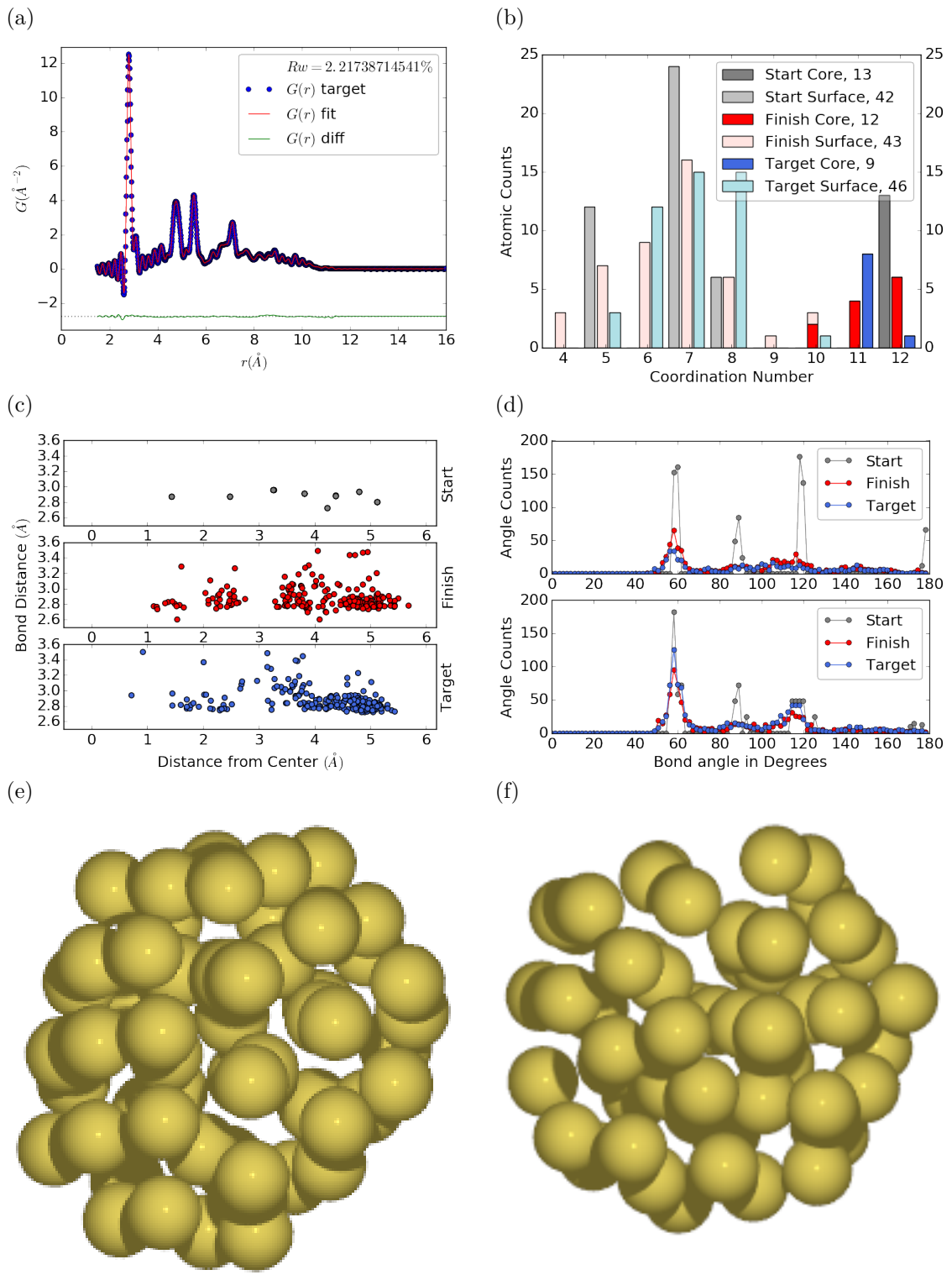


Figure 4.3: Similar to figure 4.2 for DFT-optimized amorphous Au_{55} .

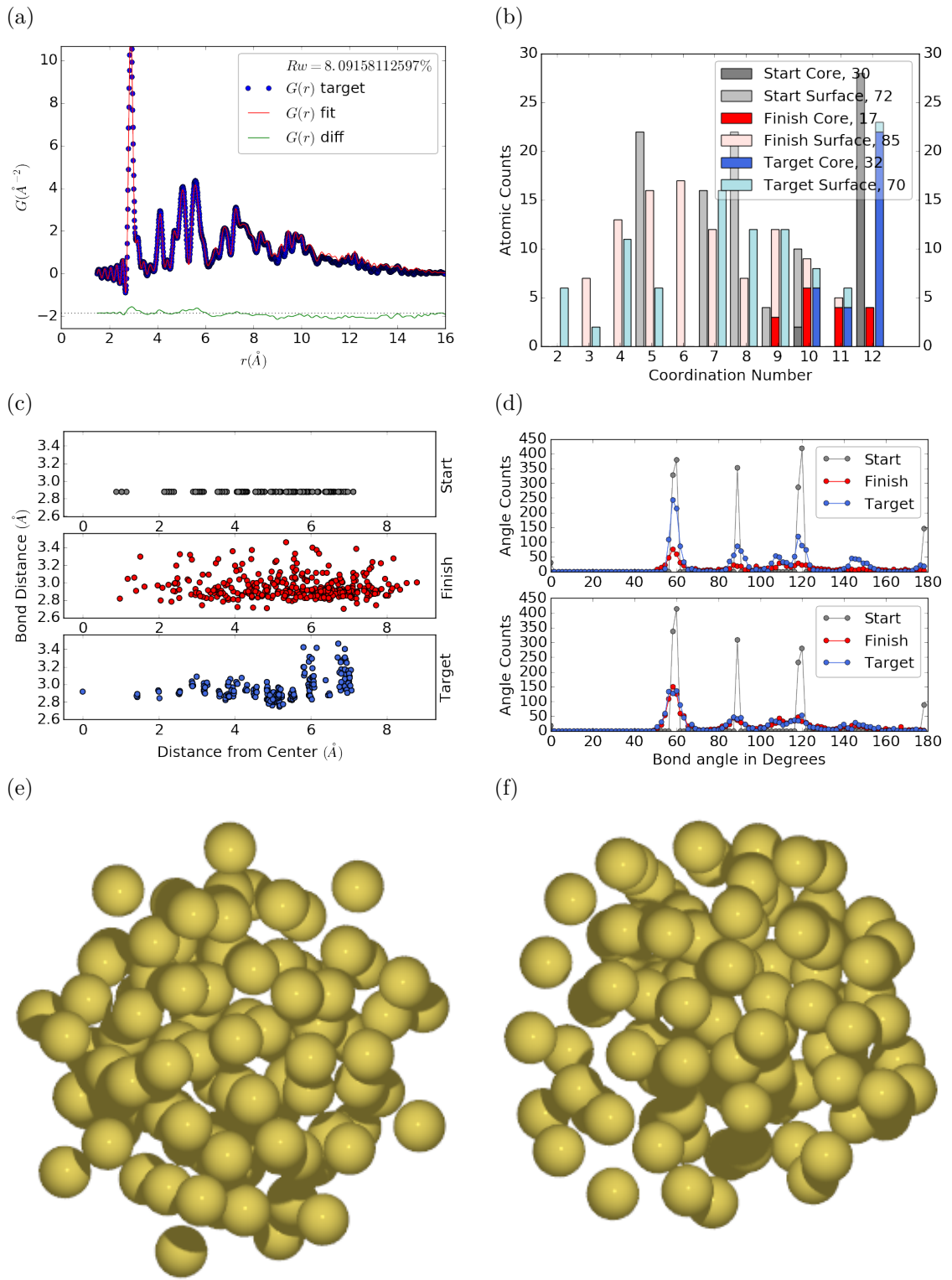


Figure 4.4: Similar to figure 4.2 for Au_{102} as in DFT-optimized $\text{Au}_{102}\text{MBA}_{44}$ cluster.

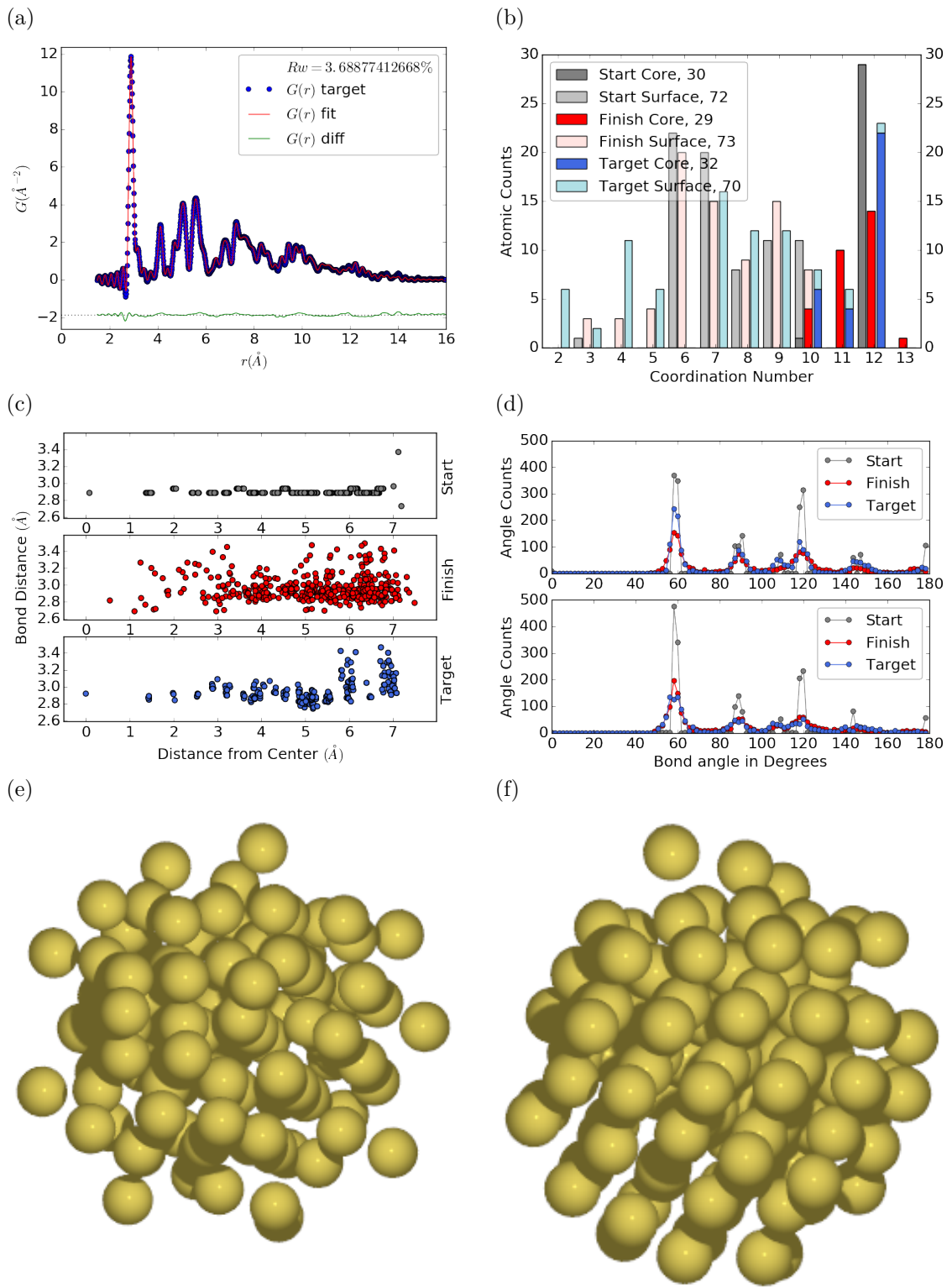


Figure 4.5: Similar to Fig. 4.4 with Marks decahedron as the starting structure.

412

CHAPTER 5

413

ANNEALING AND AGGREGATION OF 2NM

414

AU NANOPARTICLES

415 5.1 EXPERIMENTS

416 NP Synthesis

417 X-ray Total Scattering Measurements

418 5.2 DATA PROCESSING

419 5.3 DATA ANALYSIS

420 5.4 SIMULATION

421 5.5 STRUCTURAL ANALYSIS

422 5.6 CONCLUSIONS

423

CHAPTER 6

424

PHASE CHANGES AND ANNEALING DYNAMICS OF

425

Pr_2NiO_4 AND ITS DERIVATIVES

426

6.1 EXPERIMENTS

427

Pr_2NiO_4 Synthesis

428

X-ray Total Scattering Measurements

429

6.2 DATA PROCESSING

430

6.3 DATA ANALYSIS

431

Intra Sample Comparison

432

Inter Sample Comparison

433

6.4 SIMULATION

434

Small Box

435

Large Box

436

6.5 STRUCTURAL ANALYSIS

437

6.6 CONCLUSIONS

438

CHAPTER 7

439

CONCLUSION